Passive UHF RFID Tag Antenna Design Using Graphite-Based Conductive Papers

by

Michael R. Kurz

Bachelor of Science in Engineering, University of New Brunswick 2012

A Thesis, Submitted in Partial Fulfillment of the Requirements for the Degree of

Master of Science in Engineering

In the Graduate Academic Unit of Electrical and Computer Engineering

Supervisor: Bruce G. Colpitts, Ph.D., Electrical and Computer Engineering

Examining Board: Maryhelen Stevenson, Ph.D., Electrical and Computer Engineering, Chair
Yonghao Ni, Ph.D., Chemical Engineering
Brent Petersen, Ph.D., Electrical and Computer Engineering

This thesis is accepted by the
Dean of Graduate Studies

THE UNIVERSITY OF NEW BRUNSWICK

April, 2016

Abstract

The emergence of passive ultra-high frequency (UHF) radio-frequency identification (RFID) systems has led to the annual production of RFID tags in the billions. Two graphite-based solutions developed at the Limerick Pulp and Paper Research Centre (LPPRC) were identified as possible candidates to achieve a more environmentally conscious tag with less complex manufacturing methods compared to what is currently available on the market. These materials are almost entirely composed of carbon and can be formed onto a biodegradable paper substrate using relatively simple methods.

The materials' intrinsic properties are characterized and a simulation profile is created to aid in the design of an optimized tag antenna. Conductivities of 600 S/m and 39,000 S/m are measured for the two graphite-ink and exfoliated-graphite based papers, respectively.

Anechoic chamber read range measurements are performed using a commercial RFID reader. Maximum theoretical read ranges for prototype tags built using graphite-ink and exfoliated-graphite based papers are found to be 2.26 m and 6.83 m, respectively. Comparison of graphite-based tag prototypes and a commercial tag suggests that they are suitable for applications where the benefits of manufacturability and bio-degradability outweigh the disadvantage of a large antenna footprint. Six total designs with varying read ranges, complexities, sizes, and materials are found.

Dedication

To my family.

Acknowledgements

I must first thank my supervisor, Dr. Bruce Colpitts for his guidance and support over the past several years. His knowledge has been invaluable towards developing my practical and analytical skills as a young engineer. I would also like to thank him for the countless opportunities he has provided me to pursue studies in the field I truly enjoy.

I must also thank Joseph Mosseler, my friend and colleague, for his enormous contributions on the chemistry side of this project. My work would undoubtedly not exist if it wasn't for him. Just as important were our Friday afternoon Grad House discussions, which were a great motivator during the more difficult weeks.

Several others must be thanked for their help along the way: Dr. Chris Rouse, for always answering the hundreds of questions I threw at him; Dr. Brent Petersen, for giving me the opportunities to grow both inside and outside of academia; Shelley Cormier, for always know exactly who to talk to, or what to fill out. I'd also like to thank Farid Mirhosseini for our discussions on permittivity, and Ryan Jennings, for always being able to solve my technical issues quickly.

Finally, I'd like to thank my parents for their unending support throughout my entire education. Although at times it may have seemed slow I truly thank them for their patience over the past few years.

Table of Contents

List of Tables

List of Figures

List of Abbreviations and Symbols

CST MWS	Computer Simulation Technology Microwave Studio
cm	Centimetres
dB	Decibels
dBi	Decibels Relative to an Isotropic Radiator
dBm	Decibels Relative to a milliwatt
DC	Direct Current
EIRP	Effective Isotropic Radiated Power
EM	Electro-Magnetic
EPC	Electronic Product Code
FR4	Fire Resistant-4
GIC	Graphite Intercalated Compound
GSM	Grams per Square Metre
H_2SO_4	Sulfuric Acid
HF	High Frequency
Hz	Hertz
IC	Integrated Circuit
IEEE	Institute of Electrical and Electronics Engineers
LPPRC	Limerick Pulp and Paper Research Centre
m	Metres
MHz	Megahertz
MLA	Meander Line Antenna
mm	Millimetres

PC	Personal Computer
PEC	Perfect Electrical Conductor
PET	Polyethylene Terephthalate
RF	Radio Frequency
RFID	Radio Frequency Identification
RSS-247	Radio Standards Specification for Digital Transmission Systems, Frequency Hopping Systems and License-Exempt Local Area Network Devices.
S	Siemens
SDS	Silicon-based Dispersant
SKU	Stockkeeping Unit
SO_2	Sulfur Dioxide
SOT-323	Small Outline Transistor-323 package
UHF	Ultra High Frequency
USB	Universal Serial Bus
W	Watts
WPT	Wireless Power Transmission
Mm	Micrometres
a_i	Incident Power Wave
A_e	Antenna Effective Aperture Area
α	T-Match Antenna Current Splitting Factor
b_i	Reflected Power Wave
$\vec{B}$	Magnetic Flux Density Vector

C_{Power}	Effective Isotropic Radiated Power Coefficient Between Simulations and Measurements
C_{Th}	Threshold Power Coefficient Between Simulations and Measurements
d_l, d_t, d_w	Sample Length, Thickness, and Width for the Four-Point-Probe Method
$\vec{D}$	Displacement Field Vector
$D(\theta, \phi)$	Directivity
D_0	Maximum Directivity
δ_c	Skin/Penetration Depth
$\vec{E}$	Electric Field Vector
E_0	Electric Field Amplitude Maximum
e_{Rad}	Radiation Efficiency
ε	Electric Permittivity
ε'	Real Pert of Permittivity
ε''	Imaginary Part of Permittivity
ε_0	Permittivity of Free Space
ε_r	Relative Permittivity
f	Frequency
g_1	Meander Line Antenna Gap Distance
$G(\theta, \phi)$	Gain
G_{Tx}	Transmitter Antenna Gain
G_{Tag}	Tag Antenna Gain
$\vec{H}$	Magnetic Field Intensity Vector

I_s	Antenna-Tag Circuit Current
j	Imaginary Number
$\overrightarrow{J_b}$	Bound Current Density Vector
$\overrightarrow{J_f}$	Free Current Density Vector
l, l_1	Antenna Trace Lengths, Check with Section Figure
L_{Cable}	Measurement Cable Loss
λ	Wavelength
μ	Magnetic Permeability
μ_0	Permeability of Free Space
N	Number of Meanders per Radiator (Total $2N$ per Antenna)
Ω	Ohms
$\vec{P}$	Electric Polarization Vector
P_E	Exchangeable Power
$P_{E,, Inst}$	Instantaneous Exchangeable Power
P_T	Maximum Power Transferred to a Matched Load
P_{th}	Threshold Power for a Tag IC to Power on
P_{Tx}	Transmitter Output Power
ϕ	Polar Angle
r_{Max}	Maximum Read Distance
r_{Norm}	Maximum Read Distance Normalized to the Measurement Test Setup.
R	Resistance Measured Between Probes of the Sample

$R_{12,34}$	Ratio of the Voltage Between Probe Points 3 and 4 and the Current Through 1 and 2.
R_{Ant}	Antenna Input Resistance
R_{IC}	Tag Integrated-Circuit Input Resistance
R_{Loss}	Antenna Loss Resistance
R_{Rad}	Antenna Radiation Resistance
r	Distance Between Reader and Tag
ϱ_i	Kurokawa's Power Wave Correction
s_e	T-Match Separation Distance
$\|s\|^2$	Power Wave Reflection Coefficient
σ	Electrical Conductivity
σ_{eff}	Effective Electrical Conductivity
t	Conductor Thickness
$tan\ \delta_c$	Loss Tangent
τ	Tag Antenna-IC Transmission Coefficient
τ_{Tx}	Feed Line-Antenna Transmission Coefficient
θ	Azimuth Angle
V_S	Equivalent Antenna Generator Voltage
V_T	Antenna Terminal Voltage
w, w_1, w_2, w_3, w_4	Antenna Trace Widths, Check with Section Figure
W_i	Radiation Power Density of Incident Wave
ω	Angular Frequency
X_{Ant}	Antenna Input Reactance
X_{IC}	Tag Integrated Circuit Input Reactance

Z_a	Antenna Mode Input Impedance
Z_{Ant}	Antenna Input Impedance
Z_i	Generator Input Impedance
Z_{IC}	Tag Integrated Circuit Input Reactance
Z_t	Transmission Line Mode Input Impedance
Z_T	Total T-Match Antenna Input Impedance
$\parallel$	Parallel to
$\perp$	Perpendicular to

Chapter 1 Introduction

Radio-frequency identification (RFID) is a wireless technology that allows the contactless identification of electronic tags. A typical RFID system consists of a local transceiver (reader) and one or more remote transponders (tags) that contain electronic information, usually about the object they are affixed upon (Figure 1.1). These tags are generally placed on or in objects of interest such as retail goods, vehicles, pets, and humans [1]. A wide array of communication protocols, frequency bands, and tag topologies has allowed RFID to become widespread over many industrial, commercial, and retail settings.

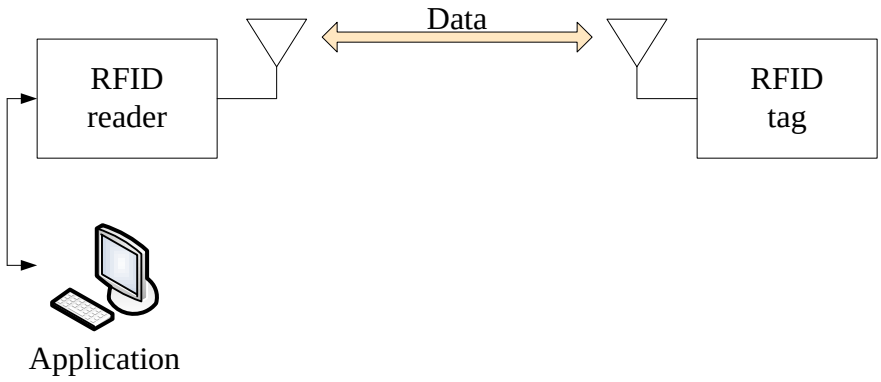

Figure 1.1: Signal flow in a simple one-reader, one-tag RFID system.

Of particular interest are the passive ultra-high frequency (UHF) RFID systems that are seeing large growth in the retail supply chain sector. These systems are characterized by extremely cheap, disposable tags that are affixed to goods to provide logistical support such as location, timestamps, origin, and serial numbers (EPCs and SKUs) to the supply chain management. Almost exclusively based on the EPC Class 1 Gen 2 standard, these electronic based tracking systems are becoming more widespread throughout the industry [2].

Passive RFID based asset tracking systems have large costs associated with the life cycle of the identifier label. In a retail setting, potentially millions of objects are tagged and sold (for practical reasons, without prior removal of the tag). This results in the necessary deployment of a new tag on every object within the supply chain. An illustration of a passive UHF RFID tag is shown in Figure 1.2.

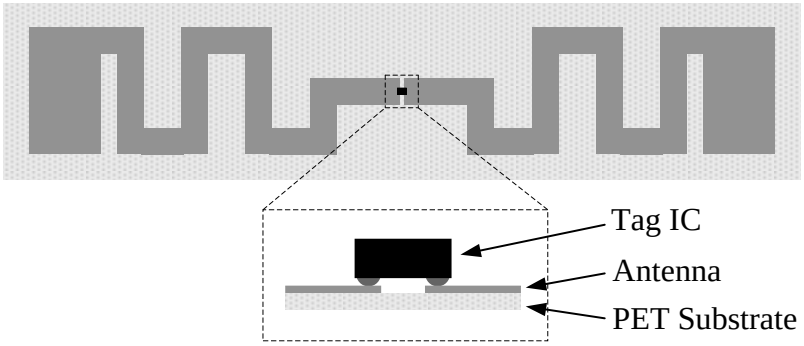

Figure 1.2: Components of a typical passive UHF RFID tag.

The tag, sometimes called a label, comprises the IC, conducting antenna elements, a substrate, and a protective structural layer. For nearly all commercially available tags, the conducting elements are made of metal, with aluminum being the most common due to its economic balance between cost and conductivity. The substrate layer is typically made from polyethylene terephthalate (PET), a plastic polymer that provides structure to the antenna and a durable surface for wet-etching. The wet-etching technique is used to form the antenna by removing metal layers until the desired shape is achieved, a time-consuming process that also generates chemical waste [3]. The PET plastic used is considerably non-biodegradable, which is an undesirable characteristic in an industry that produces nearly 4 billion tags per year [4].

Work performed at the Limerick Pump and Paper Research Centre (LPPRC) at the University of New Brunswick has yielded two conductive, graphite-based papers

which were identified as possible alternatives to traditional tags. The process used to form these materials eliminates the need for wet-etching, and replaces the plastic substrate with a paper one.

The research presented in this thesis investigates the viability of two graphite-based conductive papers as antenna materials. These materials are studied to determine if graphite-based papers can provide a more environmentally conscious alternative to traditional tag materials. The graphite materials are first characterized by their intrinsic properties and then implemented into an electromagnetic solver to facilitate the design process of the tag antennas. Prototypes are then created and compared to their predictions, and final performance results are reported.

Chapter 2 Background

Although modern RFID systems have been available for more than a decade, the technology maintains roots back to the turn of the 19th century with inventor and electrical engineer Nikola Tesla. In 1899 Tesla conducted an experiment that saw the construction of a sixty metre high coil powered by 300 kW of AC power. He successfully demonstrated the lighting of two hundred 50 W incandescent lamps 42 km away from the station [5]. This was the beginning of Wireless Power Transmission (WPT) and laid the foundation for RFID technology.

Some of the first applications of passive RFID backscatter modulation appeared during World War II in the form of "friend or foe" identification [6]. German aircraft performed synchronized roll maneuvers while British aircraft were fitted with antennas whose loads could be switched manually or electronically. Both procedures resulted in a modulated radar cross section that the base stations could use to identify the craft.

In the mid 1940s Russian inventor Léon Theremin developed an acoustically modulated backscatter system hidden within a U.S. State Department seal. This seal was presented to the U.S. ambassador in their Moscow office and was listened to by beaming UHF energy at the device from across the street. The device allowed Soviet agents to listen in on conversations held within the office and was not discovered until the 1950s, after which time it was reversed engineered by the British government.

Modern RFID systems work upon all the same principles as these pioneering experiments, however technological improvements and protocol standardization has made them an attractive option for many industrial and commercial fields, in addition to their military applications. These include but are not limited to: aerospace and aviation,

automotive, medical technology, pharmaceutical, asset tracking, oil and gas, transportation, and entertainment media. Asset tracking in particular is seeing considerable interest as it has the greatest potential to streamline supply chain and retail management. Barcode labels can be replaced by low cost RFID tags which contain all the necessary product information within their digital storage. RFID technology has been slowly replacing traditional barcode readers as asset identification and tracking methods [1].

2.1 Active and Passive Systems

An RFID system falls into one of two categories: a passive tag system or an active tag system. Active tag systems are generally used in applications where long read/write ranges are necessary (highway tolling, transport container identification, etc.) and use an onboard battery to power their electronics. An active tag is basically a fully functional radio transceiver that is only range limited by the sensitivity of the reader and tag receivers. Conversely, passive tags are powered remotely by the incident RF power harvested from the RFID interrogator, and use some form of backscatter modulation to transmit information back to the reader. These tags can be made inexpensively when compared to active tags because they do not require an expensive battery cell or complete radio electronics. The compromise is that the tag's read range is limited not by the sensitivity of the radio electronics, but by the minimum power required to turn on the tag. The read range of a passive tag is given by [7]

$$r = \frac{\lambda}{4\pi}\sqrt{\frac{P_t G_{Tx} G_{Tag} \tau}{P_{th}}} \tag{2.1}$$

where λ is the wavelength of the signal, G_{Tx} and G_{Tag} are the transmitter and tag antenna gains respectively, P_t is the transmit power, and P_{th} is the threshold or 'turn on' power of the tag. This is the minimum power that the tag IC needs to operate. τ is the power transmission coefficient, which accounts for any power loss due to a mismatch between the tag antenna impedance (Z_{Ant}) and IC impedance (Z_{IC}) and is given by [7]

$$\tau = 1 - \left|\frac{Z_{IC} - Z_{Ant}^*}{Z_{IC} + Z_{Ant}}\right|^2 = \frac{4R_{IC}R_{Ant}}{|Z_{IC} + Z_{Ant}|^2}\ , \quad 0 \leq \tau \leq 1 \tag{2.2}$$

where R_{IC} and R_{Ant} are the real part of the IC and antenna impedances, respectively. The threshold power for a typical passive RFID IC is around -18 dBm (Table A.1, Appendix A). Maximizing the power to the IC is therefore the most important factor when designing a tag. A mathematical derivation of the equations describing read range and power transfer coefficient is performed in the section 4.1.

2.2 Review of Relevant Literature

A review of the current state of the conductive paper based antennas field was performed by the author. A thorough search of the literature available online and in print yielded a number of papers related to the use of graphite as a conductive material and radiator.

A substantial amount of information can be found concerning the use of paper as a substrate for 'printed-on' antennas in the HF and UHF range of frequencies. This research has generally been conducted to produce cheaper and more environmentally friendly alternatives to the traditional polyethylene terephthalate (PET) plastics used. Parameters such as dielectric constant (ε) and loss tangent (δ) are determined in detail, both of which are necessary for the design of substrate-mounted antennas. These values

are given for typical paper and corrugated cardboard material compositions, in addition to numerous antenna simulations demonstrating their radiation performance [8-10]. It should be noted that although the author has selected these three references, many papers have reported on this topic as it has been an area extensively researched. The values for these intrinsic material properties give a good guideline for the design work to be performed for this thesis as the substrate used in the current manufacturing process of the conductive paper is, in fact, paper.

Conductive ink based on suspended silver nanoparticles has been shown to perform well as a radiator in UHF RFID antennas [11-14]. The authors have shown that the ink/pastes can be applied into suitable geometries using inkjet printing or screen printing techniques. These techniques offer a simpler alternative to the traditional etching process of copper, as well as the added benefit of lower material costs.

Carbon-based materials have been investigated as radiating antenna elements for their advantages over copper and aluminum [15-19]. These advantages include reduced material cost, fabrication complexity, and weight, in addition to being corrosion resistant [18]. Carbon has also been used in its Polypyrrole form as a component of electrically conductive composite pulp fibres, which claim to be comparatively as biodegradable as regular cellulose fibres [19]. Reinforced carbon fibre has been demonstrated as an antenna element material with relatively good radiation characteristics when compared to metal [18]. Radiation efficiencies of up to 94% were achieved using closely spaced, braided carbon fibres.

Intercalated graphite (crystalline carbon doped with bisulphate ions) has been demonstrated as an RF patch antenna radiator, although no metrics were reported with the results [17].

Much of the motivation behind the author's proposed research has come from the work being performed at UNB's Limerick Pulp and Paper Research Centre. First generation conductive papers using Polypyrrole engineered pulp fibre were tested as antenna elements with limited success [18, 20]. Experimental work measured the gain of a purely pulp-paper based dipole at -11 dB with a corresponding radiation efficiency of 5%. These numbers are prohibitive for practical applications, however simulation work performed in the report suggests 500 Siemens per metre (S/m) as a reasonable conductivity (σ) target for acceptable radiation performance. The van der Pauw method was identified as a means of producing accurate and repeatable results for measuring the conductivity of the paper samples and will be employed in the author's research [21].

Chapter 3 Graphite Material Characterization

The work done over the past three years at the Limerick Pump and Paper Research Centre (LPPRC) has produced a number of materials suitable for practical analysis as radiating antenna elements in RFID systems. The first polymer-pulp based material was discussed in the section 2.2 and had marginal conductivity and thus was not found to be of any practical use [18, 20]. Subsequent developments produced two new materials, a graphite based ink that could be coated over a paper substrate, and an exfoliated-graphite powder that is pressed onto a structural paper base.

To determine the electromagnetic radiation characteristics of these papers or any material, there are three intrinsic properties that must be determined to solve the governing (Maxwell's) equations: conductivity, electric permittivity, and magnetic permeability. The chemical compositions of each graphite material are first described, followed by the measurements and assumptions used to determining the three necessary properties.

3.1 Graphite Paper Composition

Graphite is a crystalline allotrope of carbon that is formed of multiple graphene sheets layered on top of each other (Figure 3.1). Graphene itself is a single two-dimensional sheet of hexagonally connected carbon atoms. Each carbon atom shares a single covalent bond between its three neighboring atoms, with the last of its four valence electrons being free to migrate the plane. This characteristic makes the graphite sheets highly electrically conductive in directions along their planes but not between them. Many small flakes of these graphite sheets (called crystalline flake graphite) connected in a randomly oriented fashion form what is commonly known as graphite. As a result of this composition

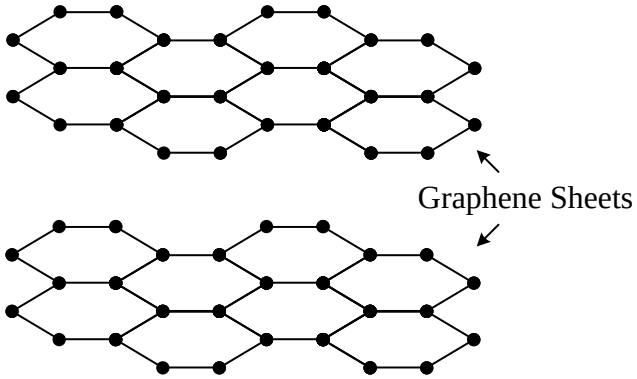

Figure 3.1: Molecular carbon-lattice structure of graphite.

graphite shares the electrically conductive property of crystalline flake graphite and exhibits this property isotropically.

The graphite ink is an air-cured liquid that is coated on to standard 75 grams per square-metre (GSM) paper, which supplies a flexible structural base (Figure 3.2). The thickness of the dried conducting layer is dependent on the viscosity of the uncured ink and the apparatus used for coating.. The cured ink is around 84% pure carbon in the form of graphite, with the remaining constituents being silicon based dispersant (SDS), latex binder, and antifoaming agent.

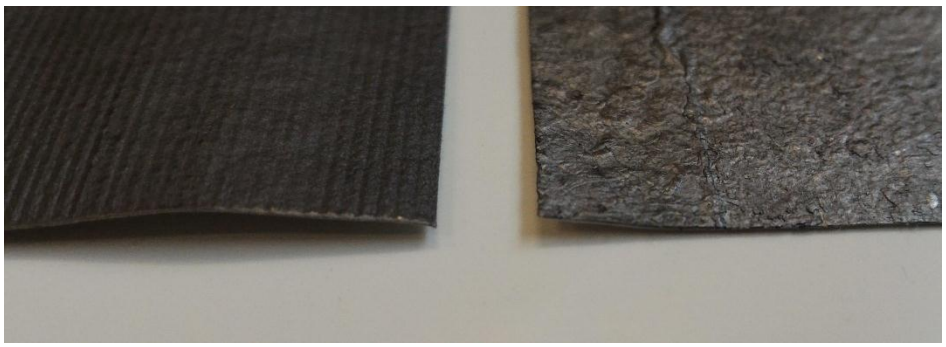

Figure 3.2: Close-up view of graphite-ink (left) and exfoliated-graphite (right) based papers.

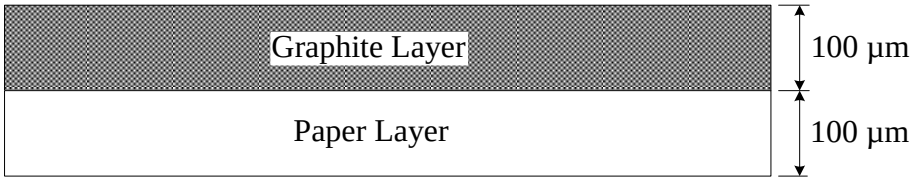

Figure 3.3: Cross-sectional view of the graphite-paper samples.

The conducting graphite layer is on average 100 µm thick, with the same thickness for the paper layer it is cured upon (Figure 3.3). The conducting layer thickness can vary based on the accuracy of the ink preparation and the repeatability of the coating apparatus, however all measured values fell between ±20% of this nominal value.

The second of the conducting graphite-based materials, exfoliated graphite, uses a similar, but larger flake graphite powder, however a completely different method of paper-forming is used. The graphite is first mixed with sulfuric acid (H_2SO_4) and potassium permanganate to create a graphite intercalated compound (GIC) and then allowed to dry. This compound is then quickly heated in an RF oven, causing the inter-layer sulfuric acid to volatilize (expelling SO_2), pushing apart the individual graphene layers. The result is a light and fluffy material, composed of many small snake-like fibres, usually a few millimetres in length. These long fibres are formed when the small flakes of tightly packed graphene sheets are forced away from each other perpendicular to their long plane. The now exfoliated graphite is then compressed onto a paper substrate using a heavy roller to form a collection of tightly packed, randomly oriented graphene sheets. The result is a thin layer of exfoliated graphite which exhibits exceptionally high conductivity.

The terms ‘graphite-ink paper’ and ‘exfoliated-graphite paper’ will herein be used to refer to the total product of their respective conducting layer and the paper substrate.

These two graphite paper materials represent the best of the carbon based solutions that have come out of the research at the LPPRC in terms of conductivity, durability, and manufacturability. The graphite-ink paper has lower conductivity and is relatively easy to fabricate while the exfoliated-graphite paper has higher conductivity, but involves more complicated manufacturing steps. These characteristics will be considered in conjunction with their radiation performance to determine each material's overall merit for RFID applications.

3.2 Conductivity Measurements

To model an antenna with any electromagnetic solver the electrical conductivity σ must be known so Maxwell's equations can be evaluated at a point in space. Conductivity is a measure of a material's capacity to support an electric current density $\overrightarrow{J_f}$ in the presence of an electric field $\vec{E}$. This relationship is discussed further in section 3.3, however for a good conductor it can be considered frequency independent and is mathematically given by [22]

$$\overrightarrow{J_f} = \sigma\vec{E} \tag{3.1}$$

A higher conductivity results in a higher current for a given electric field, and lower resistive (heat) losses in the material. Because the conductivity is the same for a DC excitation as it is for 915 MHz, it can be measured without complex high-frequency equipment [22]. There are two well established methods for measuring conductivity of a material: the classical four-point-probe method and the van der Pauw method [21]. The classical four-point-probe method uses a bar shaped sample of the material, a current

contact at each end of the sample, and two voltage probes positioned as shown in Figure 3.4.

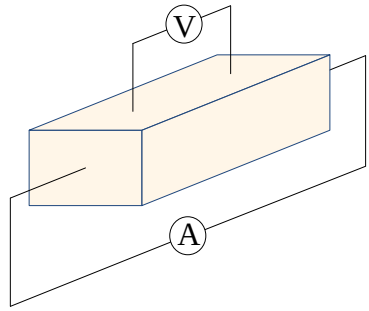

Figure 3.4: Four-point-probe method of measuring conductivity.

The conductivity is derived from the current, voltage drop, and geometry of the sample. The current contacts must be far enough away from the voltage probes to ensure that the current flow is sufficiently parallel and evenly distributed throughout the sample. Conductivity is calculated using the following equation:

$$\sigma = \frac{d_l}{R d_w d_t} \tag{3.2}$$

where R is the ratio of the voltage drop across the probes to the current through contacts, and d_l, d_w, and d_t are the length, width, and thickness of the sample, respectively.

The van der Pauw method is similar to the four-point-probe method in that it uses a pair of current contacts and a pair of voltage probes to determine the conductivity of a sample. The difference lies in the fact that it can be used for a sample of arbitrary shape, provided it is sufficiently flat with its width being much larger than its thickness. This characteristic is achieved by the use of conformal mapping, with a full derivation found in [21]. To calculate the conductivity from the voltage and current measurements of a sample the following equation is used.

$$e^{-\pi\sigma d_t R_{12,34}} + e^{-\pi\sigma d_t R_{23,41}} = 1 \tag{3.3}$$

The resistance $R_{12,34}$ is defined as the ratio of the voltage drop across points 3 and 4 to the current through contacts 1 and 2. The resistance $R_{23,41}$ is similarly defined. With these values and the knowledge of the sample thickness d_t, Equation (3.3) can be solved recursively to determine a value of conductivity.

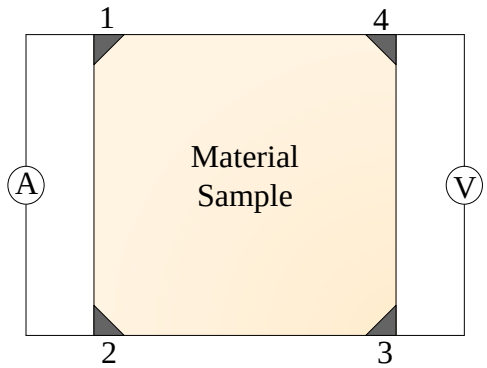

Figure 3.5: Van der Pauw method of measureing conductivity.

Both methods discussed were used to identify a nominal value of conductivity and if there was a close agreement between the two methods. Table 3.1 shows the results of the conductivity measurements.

From the results in Table 3.1 it can be seen that there is close agreement between the conductivities of the exfoliated graphite, but an obvious difference between those of the graphite ink. This is due to the occurrence of small, elevated ridges on the graphite layer which develop during the coating process. These ridges are a result of the wound rods used in the coating machine and are unavoidable without drastically altering the chemical formula and compromising the conductive quality of the ink. Conductivity is an intrinsic material property (independent of the material's geometry), however to experimentally determine it, the thickness of the sample must be known. The ridges produce a non-uniform thickness, making the calculation of the conductivity difficult. To

Table 3.1: Measurement results for conductivity tests of graphite-ink and exfoliated-graphite papers.

Graphite Ink Conductivity (S/m)		Exfoliated Graphite Conductivity (S/m)	
Van der Pauw	Four Point Probe	Van der Pauw	Four Point Probe
654.4	⊥ to ridges: 487.2 ∥ to ridges 602.3	39,225	38,013
Nominal: 600		Nominal: 39,000	

simplify the process the conductivities were measured in the directions parallel and perpendicular to the ridges using the nominal thickness measured by a set of calipers, averaged, and rounded. This provides the average conductivity for the nominally 100 µm thick sample.

3.3 Permittivity

In section 3.2 it was stated that the graphite papers can be considered a good conductor. To substantiate this claim, a careful treatment of the material's permittivity must be considered. When an electric field is present in a bulk material the atoms and molecules that comprise the medium will tend to gain an electric dipole moment that aligns with the applied electric field. In a dielectric, this alignment of small electric dipoles does not result in a net charge inside the material; however, a small surface charge does appear on the surface of the material (Figure 3.6). The amount of surface charge is a direct indicator of the overall electric polarizability of the material.

The total electric dipole moment a material can gain can be explained by three atomic mechanisms. Electronic polarizability describes the behavior of a single atom

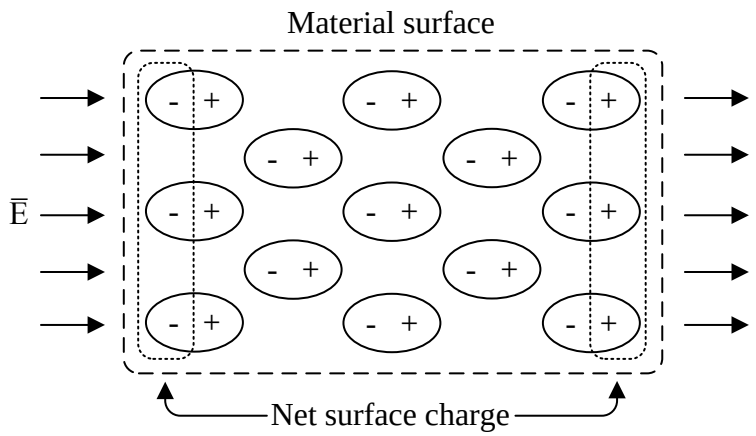

Figure 3.6: Dipole alignment in a material due to an applied electric field.

under the influence of an applied electric field. The electric field pulls the positively charged atom nucleus away from the centre of its negatively charged electron cloud, resulting in an overall dipole moment on the atom.

Many molecules are made up of two or more positively or negatively charged ions forming covalent or ionic bonds. Ionic polarizability arises from an electric field displacing these individual ions within the overall structure of the molecule.

In addition to being ionically polarizable, some molecules, such as H_2O, may also carry a permanent dipole moment. This is caused by the relative position and electronegativity of the individual atoms that compose the molecule. Typically in a material these permanent dipole moments point in random directions; however when an electric field is applied they tend to align with the field. Kinetic collisions typically prevent the alignment of very large numbers of polarized molecules, keeping the overall orientation polarization contribution on par with that of electronic and ionic polarization [23]. All three of these effects are linked to the resonance of the atomic structure, meaning the polarizability is inherently frequency dependent.

The electric dipole moments are bound atomically and can never actually be separated past atomic distances. This results in a distinct difference from the conduction current in a medium, the latter of which is caused by the flow of free charges (electrons) from one atom to another. These bound charges only maintain continuous movement above DC frequencies where their back and forth motion under the effect of an applied electric field constitutes a current. This current is appropriately named the displacement current and gives rise to the corresponding electric displacement field D. It was Maxwell who, in 1861, added this term into Ampère's law and unified the family of equations that describe electromagnetic behavior known today as Maxwell's equations [23]. Maxwell was also the first to note that the displacement field must also exist in free space (a vacuum) to properly predict the behavior of propagating EM waves. From these observations Maxwell deduced that the total displacement field $\vec{D}$ is given by a free space term in addition to an electric polarization term $\vec{P}$, the latter of which is a characteristic of the propagation medium.

$$\vec{D} = \varepsilon\vec{E} = \varepsilon_0\vec{E} + \vec{P} \tag{3.4}$$

where ε is the permittivity of the material and ε_0 is the permittivity of free space. Permittivity is a measure of a bulk material's tendency to resist the forming of an electric field within itself. It will later be shown that the permittivity can be used to describe both displacement (bound) and conduction (free) currents using complex notation. It should be noted that $\vec{P}$ is a macroscopic quantity that describes all three polarization mechanisms in a specific material. Permittivity can be related to the electric polarization by [22].

$$\vec{P} = \varepsilon_0(\varepsilon_r - 1)\vec{E} \tag{3.5}$$

where $\varepsilon_r$is the permittivity of the material relative to that of free space (ε_0) and $\vec{E}$ is the electric field vector.

$$\varepsilon = \varepsilon_0 \varepsilon_r \tag{3.6}$$

Maxwell's fourth equation, Ampère's law, describes the relationship between a current and its corresponding magnetic field $\vec{H}$. It should be noted by the reader that in literature the term magnetic field can be used to refer to both the $\vec{B}$ and $\vec{H}$ field, therefore they will herein be explicitly referred to as either the $\vec{B}$ field or $\vec{H}$ field. Ampère's law is given by

$$\nabla \times \vec{H} = \vec{J_f} + \frac{\partial \vec{D}}{\partial t} \tag{3.7}$$

where J_f is the current density contributed by the free charges (electrons) in the bulk material. The curl of the $\vec{H}$ field is influenced by both the free charges and the bound charges (polarization).

In a dielectric the current density contribution from free charges is relatively small (zero for lossless dielectric) so the total current density is dominated by the displacement current. Conversely, in metals, the free current dominates the displacement current, which tends to simplify the governing equations. It is important to note that these assumptions are based on the value of permittivity for the material under question. Graphite paper lies somewhere in the middle of these two extremes therefore a mathematical treatment of Ampère's law will suggest what, if any, simplifications can be made.

For UHF RFID, the operating frequency band is a very small percentage (less than 3%) of the operating frequency. In such cases it is helpful to look at the time

harmonic (steady state sinusoidal) form of Maxwell's equations. This time harmonic form of Ampère's law can also be considered the phasor form and is given by

$$\nabla \times \vec{H} = \vec{J_f} + j\omega\vec{D} \tag{3.8}$$

Substituting for $\vec{D}$ yields

$$\nabla \times \vec{H} = \vec{J_f} + j\omega\varepsilon\vec{E} \tag{3.9}$$

Permittivity ε is a complex value, where the imaginary part accounts for the loss (as heat) in a material due the dielectric damping of electric polarization effects. Mathematically, the permittivity can be written as

$$\varepsilon = \varepsilon' - j\varepsilon'' \tag{3.10}$$

The conduction (or free) current density is determined by a material's conductivity, σ, as [24]

$$\vec{J_f} = \sigma\vec{E} \tag{3.11}$$

Substituting the preceding two equations into the expanded form of Ampère's law yields

$$\nabla \times \vec{H} = \sigma\vec{E} + j\omega(\varepsilon' - j\varepsilon'')\vec{E}$$

$$\nabla \times \vec{H} = \sigma\vec{E} + \omega\varepsilon''\vec{E} + j\omega\varepsilon'\vec{E}$$

$$\nabla \times \vec{H} = (\sigma + \omega\varepsilon'')\vec{E} + j\omega\varepsilon'\vec{E} \tag{3.12}$$

It can be seen that σ and ε''produce the same effect on the conduction current, and can be lumped together as an effective conductivity.

$$\sigma_{eff} = \sigma + \omega\varepsilon'' \tag{3.13}$$

It should be noted that although the effective conductivity of a material is frequency dependent the conductivity is not, and is simply the ratio of the conduction current density to the electric field strength in a bulk material for any frequency including DC (0

Hz). The loss tangent δ_c is a measure of the relative magnitudes of σ_{eff} and $\omega\varepsilon'$ and is given by

$$\tan\delta_c = \frac{\sigma_{eff}}{\omega\varepsilon'} = \frac{\sigma + \omega\varepsilon''}{\omega\varepsilon'} \tag{3.14}$$

A material is considered a good conductor when $\tan\delta_c \gg 1$ and a good insulator (dielectric) when $\tan\delta_c \ll 1$ [23]. The permittivity of pure graphite, taken from the CST MWS material library and confirmed in [25], is around ε = 12 – j15 and the conductivity of the graphite-ink-based paper is 600 S/m. Calculating the loss tangent for the graphite paper at 915 MHz yields:

$$\tan\delta_c = \frac{\sigma_{eff}}{\omega\varepsilon'} = \frac{600\frac{S}{m} + (2\pi \times 915 \times 10^6 Hz)\left(15 \times 8.85 \times 10^{-12}\frac{s^4A^2}{m^3kg}\right)}{(2\pi \times 915 \times 10^6 Hz)\left(12.5 \times 8.85 \times 10^{-12}\frac{s^4A^2}{m^3kg}\right)} = 938.7$$

It is very clear that graphite is a good conductor under the criteria given in [23]. Applying a similar treatment to Ampère's law yields:

$$\nabla \times \vec{H} = \sigma_{eff}\vec{E} + j\omega\varepsilon'\vec{E}$$

$$= 600.8\vec{E} + j0.64\vec{E}$$

This is effectively the same comparison as the $\tan\delta_c$ ratio; however, it explicitly shows that the real part of the right hand side dominates the imaginary part. The relationship is even more apparent for the exfoliate-graphite material (σ = 39,000 S/m). This implies that for graphite based papers, which are 80%+ pure graphite by weight, the total current in the medium can be described by

$$\overrightarrow{J_{tot}} = \overrightarrow{J_f} + \overrightarrow{J_b} \cong \sigma\vec{E} \tag{3.15}$$

This simplification can be used to facilitate modeling of the material in simulation software and determining skin depth.

The magnetic permeability is also determined by the atomic structure of the material, however for all non-ferromagnetic materials the paramagnetic and diamagnetic contributions are extremely small, and it is very common to assume a permeability equal to that of free space [23].The paper materials are non-ferromagnetic as they do not contain iron, nickel, cobalt, or manganese and satisfy this assumption ($\mu = \mu_0$).

Chapter 4 Antenna Design: Simulations

Designing antennas for UHF RFID systems presents a number of challenges unique within the antenna design field. Traditionally, an antenna structure is made to be resonant, which results in a purely real impedance that matches well to the typical 50 and 75 Ω transmission lines used for radio applications. This is also true of most transceivers, which are generally equipped with 50 Ω inputs and outputs. RFID tags, however, present a complex impedance at the terminals of the IC that is composed of a small real resistance (around 30 Ω) and a larger capacitive reactance (around -j200 Ω). For optimal power transfer the tag antenna must be matched to the complex conjugate of the IC impedance, so an antenna with a large inductance is desirable. The theory behind optimal power transfer will be presented in this chapter, along with the various techniques used in designing planar RFID tag antennas.

In a commercial field such as RFID, read range performance is but one of the metrics used to determine how good a tag is. Other characteristics of a good tag include minimizing the physical tag area (footprint), maintaining a practical manufacturing process, and equalizing the radiation directivity. Equalizing the directivity is equivalent to making the antenna radiate isotropically, reducing the number of angles from which the tag becomes electromagnetically invisible. Each of these is generally a compromise and will be considered throughout the design process. A maximum antenna width of one centimetre was imposed, to keep the footprints on par with those of most commercial tags, however all other parameters were unlimited.

4.1 Power Optimization

The RFID tag antenna is the component of the tag that converts electromagnetic radiation into an IC compatible electrical signal. These antennas can vary widely in design based on their operating frequency and their principle of operation (near or far-field), however all must be impedance matched to their terminating IC for efficient power transfer [26]. Designing these antennas is therefore a process of developing an efficient radiating structure and using impedance matching techniques to ensure maximal power transfer between the antenna and tag IC.

The front end of the tag IC contains the circuitry that allows the conversion of ultra-high frequency RF power into DC power to energize the onboard logic. Typically this is a charge pump rectifier structure that is composed of capacitors and diodes or diode connected transistors [5]. These devices are inherently capacitive and thus present a negative reactance value. The input impedance of many commercially available tag ICs can be found in Table A.1, Appendix A. Due to the topology of the rectifier circuit the IC input impedance is a function of frequency and input power level. To simplify the design process, manufacturer's report an equivalent parallel input capacitance and resistance at a specific power level (usually around the threshold sensitivity for the chip).

In order to treat any antenna mathematically it is assigned an input impedance, which is defined as the ratio of the voltage to the current at its terminals. When the antenna is operated in transmitting mode (antenna connected to a generator) the input impedance simply acts as a load on the generator. When operated in receiving mode (antenna connected to a load) the input impedance acts as an internal resistance of a

source connected to a load. For passive UHF RFID tags the antenna-IC connection is modeled in the receiving antenna mode and is shown in Figure 4.1 [24].

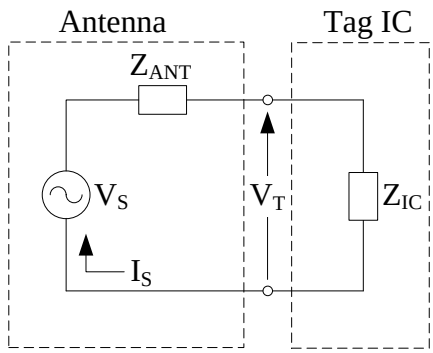

Figure 4.1: Electrical schematic of an RFID Tag in receiving mode.

The input impedance Z_{Ant} is generally a complex number that characterizes the magnitude ratio and phase differences between the voltage and current at the antenna terminals. Both complex impedances can be broken down into their real resistance and imaginary reactance parts:

$$Z_{Ant} = R_{Ant} + jX_{Ant}. \tag{4.1}$$

$$Z_{IC} = R_{IC} + jX_{IC}. \tag{4.2}$$

The power available to a load IC is a function of the antenna's effective aperture area and the intensity of the electromagnetic plane wave incident to the antenna [24]. This is given by

$$P_T = A_e W_i \tag{4.3}$$

where A_e is the effective area (m^2) of the antenna and W_i is the power density of the incident wave (W/m^2). The effective area is thus a simple way of determining how much RF power an antenna can collect, with a larger A_e resulting in more received power and a better antenna. The effective area is also given by [24]

$$A_e = \left(\frac{\lambda^2}{4\pi}\right) G(\theta, \phi) = e_{Rad} \left(\frac{\lambda^2}{4\pi}\right) D(\theta, \phi) \tag{4.4}$$

where $G(\theta, \phi)$ and $D(\theta, \phi)$ are the gain and directivity of the antenna in the direction $\{\theta, \phi\}$, respectively, and e_{Rad} is the radiation efficiency of the antenna. The radiation efficiency is defined as the ratio of the radiation resistance over the sum of the radiation and loss resistance in the antenna. The radiation resistance is a virtual resistor that models the power lost due to the radiation of RF energy from the antenna while the loss resistance models the energy dissipated as heat within the conductor and any surrounding dielectrics. Mathematically this is given by

$$e_{Rad} = \frac{R_{Rad}}{R_{Ant}} = \frac{R_{Rad}}{R_{Rad} + R_{Loss}} \tag{4.5}$$

A radiation efficiency of 1 is desirable and implies that all of the power entering the antenna is radiated while none is lost as heat. It should be noted that the real part of the antenna's input impedance R_{Ant} is the sum of the radiation resistance and the loss resistance. Combining Equations (4.3), (4.4), and (4.5) gives the maximum exchangeable power P_E of an antenna.

$$P_E = \frac{R_{Rad}}{R_{Rad} + R_{Loss}} \left(\frac{\lambda^2}{4\pi}\right) D(\theta, \phi) W_i \tag{4.6}$$

The directivity is defined in all directions pointing radially outwards from the centre of the antenna however it is convenient to simplify the expression by looking only at the maximum value (D_0), which occurs when θ = 0 for an ideal (infinitely thin wire) dipole structure. In other words, the maximum directivity occurs in the direction perpendicular to and centered on the long axis of the antenna. It has been shown that for conductivities above 100 S/m the maximum directivity for a half-wave dipole is approximately +2.2 dBi

[20]. The optimization process will presumably result in an antenna that is not an exact half-wavelength long, necessitating consideration of the exact directivity for other antenna geometries.

Equation (4.6) states the power delivered to a matched load (conjugate impedance match); however the more general case of any load impedance is of more interest. A convenient way to analyze the power mismatch in a generator-load circuit is by the use of power waves. This technique was first suggested by Penfield [27] in 1960 and later generalized for all impedances by Kurokawa [28] in 1965. Kurokawa defines two power waves (redefining nomenclature to agree with Figure 4.1) as

$$a_i = \frac{V_T + Z_{Ant} I_S}{2\sqrt{|Re\{Z_{Ant}\}|}}, \qquad b_i = \frac{V_T - Z_{Ant}^* I_S}{2\sqrt{|Re\{Z_{Ant}\}|}} \tag{4.7, 4.8}$$

where $Re\{\}$ and $*$ denote the real value and complex conjugate operators, respectively. The two waves a_i and b_i are referred to as the incident and reflected power waves between the source and the load respectively. Applying Kirchhoff's voltage law to the circuit in Figure 4.1 and substituting into the expression for a_i yields

$$|a_i|^2 = \frac{|V_S|^2}{4|R_{Ant}|} = P_E \tag{4.9}$$

where P_E is the instantaneous exchangeable power, or the maximum power available to a load. In general, Kurokawa gives the instantaneous exchangeable power as

$$P_{E,Inst.} = \varrho_i |a_i|^2$$

where ϱ_i is defined by

$$\varrho_i = \begin{cases} 1 & when\ Re\{Z_i\} > 0 \\ -1 & when\ Re\{Z_i\} < 0 \end{cases}$$

However, for all passive devices such as antennas $Re\{Z_i\} > 0$, thus $\varrho_i = 1$. Using the identities $|A| = \sqrt{AA^*}$ and $Re\{A\} = \frac{1}{2}(A + A^*)$ it was shown that [28]

$$\frac{|a_i|^2 - |b_i|^2}{2} = \frac{\varrho_i Re\{V_T I_S^*\}}{2} = \frac{1}{2} Re\{V_T I_S^*\} = P_{IC} \tag{4.10}$$

where $\frac{1}{2} Re\{V_T I_S^*\}$ is equivalent to the average power (for a sinusoid excitation) delivered to the load IC. The power wave reflection coefficient s is defined as the ratio of the power waves b_i and a_i; and, following substitution with Equations (4.7), (4.8) and the relation $V_T = Z_{IC} I_S$, is given in terms of the antenna and load impedances.

$$s = \frac{b_i}{a_i} = \frac{Z_{IC} - Z_{Ant}^*}{Z_{IC} + Z_{Ant}} \tag{4.11}$$

Taking the square of the absolute value of this expression yields the power reflection coefficient

$$|s|^2 = \left|\frac{b_i}{a_i}\right|^2 = \frac{|b_i|^2}{|a_i|^2} = \left|\frac{Z_{IC} - Z_{Ant}^*}{Z_{IC} + Z_{Ant}}\right|^2 \tag{4.12}$$

This coefficient corresponds to how much of the incident power is reflected away and not absorbed by the load. The power is not reflected in the true sense that an EM wave on a transmission line might be (there is no transmission line present to support a reverse travelling wave) but is simply a handy convention to describe power not delivered to the load due to an impedance mismatch. The power reflection coefficient can only take on values between 0 and 1 corresponding to the case of a perfect conjugate match, and a complete load mismatch (open or short load), respectively. Combining Equations (4.10) and (4.12) yields:

$$P_{IC} = \frac{|a_i|^2 - |s|^2 |a_i|^2}{2} = P_E - |s|^2 P_E = P_E(1 - |s|^2) \tag{4.13}$$

Equation (4.13) is important because it states that the maximum power delivered to the load is equal to the exchangeable power while the minimum is zero watts. Combining Equations (4.6) and (4.13) yields the total power transferred to the load for any load impedance.

$$P_T = \frac{R_{Rad}}{R_{Rad} + R_{Loss}} \left(\frac{\lambda^2}{4\pi}\right) D(\theta, \phi)(1 - |s|^2) W_i$$

$$P_T = \frac{R_{Rad}}{R_{Rad} + R_{Loss}} \left(\frac{\lambda^2}{4\pi}\right) D(\theta, \phi) \left(1 - \left|\frac{Z_{IC} - Z_{Ant}^*}{Z_{IC} + Z_{Ant}}\right|^2\right) W_i \tag{4.14}$$

The maximum read range of a given RFID tag occurs when the received tag power is equal to the minimum threshold power P_{Th} required for the tag IC to operate. Furthermore, the read range can be generalized for any transmitting (reader) antenna at a distance r from the tag antenna by the following relationships involving W_i:

$$U(\theta, \phi) = \frac{P_{Tx} G_{Tx}(\theta, \phi)}{4\pi} \tag{4.15}$$

$$W_i = \frac{U(\theta, \phi)}{r^2} \tag{4.16}$$

where $U(\theta, \phi)$ is defined as the radiation intensity in the $[\theta, \phi]$ direction and P_{Tx} is the power delivered to the transmitting antenna. Combining Equations (4.14), (4.15), and (4.16), setting $P_T = P_{Th}$, and rearranging yields an expression for the maximum read range of the tag.

$$P_{Th} = \frac{R_{Rad}}{R_{Rad} + R_{Loss}} \left(\frac{\lambda^2}{4\pi}\right) D(\theta, \phi) \left(1 - \left|\frac{Z_{IC} - Z_{Ant}^*}{Z_{IC} + Z_{Ant}}\right|^2\right) \frac{P_{Tx} G_{Tx}(\theta, \phi)}{4\pi r^2}$$

$$r_{Max} = \frac{\lambda}{4\pi} \sqrt{\frac{\frac{R_{Rad}}{R_{Rad} + R_{Loss}} D(\theta, \phi) \left(1 - \left|\frac{Z_{IC} - Z_{Ant}^*}{Z_{IC} + Z_{Ant}}\right|^2\right) P_{Tx} G_{Tx}(\theta, \phi)}{P_{Th}}}$$

$$r_{Max} = \frac{\lambda}{4\pi}\sqrt{\frac{G_{Tag}(\theta,\phi)\left(1-\left|\frac{Z_{IC}-Z_{Ant}^{*}}{Z_{IC}+Z_{Ant}}\right|^{2}\right)P_{Tx}G_{Tx}(\theta,\phi)}{P_{Th}}} \tag{4.17}$$

For nearly all passive RFID applications maximizing the received power results in the highest read range so maximizing (4.17) is imperative. From visual inspection of Equation (4.17) it can be seen that for fixed e_{Rad}, λ, P_{Tx}, G_{Tx}, and $D(\theta,\phi)$, r is largest when $Z_{Ant} = Z_{IC}^{*}$ ($R_{Ant} = R_{IC}$ and $X_{Ant} = -X_{IC}$). In other words, the read range is maximized when the antenna and IC impedances are complex conjugates of each other. The transmitting antenna gain and power are independent of the receiving tag antenna and can always be treated as constants. In general, the power transmission coefficient, radiation efficiency, and directivity are all dependent on the antenna geometry, the antenna material, and operating frequency. The antenna input impedance is, however, the most controllable parameter; so as a general design rule the input impedance should be as close as possible to the complex conjugate of the tag IC while maintaining a high radiation efficiency and a suitable directivity for the application. Equation (4.17) is equivalent to the read range equation (2.1) given in the introduction of this manuscript.

From Figure 4.1 one can see that even with conjugate matching the same current that flows though the IC also flows through the antenna resistance, dissipating power. Physically, this is the antenna re-radiating part of incident power into space and cannot be helped. From the conjugate matched case it follows that the best matched antenna for any given load is still only 50% efficient, with half the power being re-radiated [26].

4.2 Skin Depth

An important factor in the radiation performance of any conductive material is its penetration depth or skin depth, which affects the resistance experienced by any current flowing through it. Formally, the skin depth is defined as the distance into a material which an EM wave will attenuate to $1/e$ or 36.8% of its original intensity at the surface. The general expression is given mathematically by [29]

$$\delta_g = \frac{1}{\omega\sqrt{\frac{\mu\varepsilon}{2}\left(\sqrt{1+\frac{\sigma^2}{\omega^2\varepsilon^2}}-1\right)}} \tag{4.18}$$

where ω is the angular frequency of the EM wave, and μ, ε, and σ are the permeability, permittivity, and conductivity of the material, respectively. For good conductors, this expression can be reduced to [29]

$$\delta_c = \sqrt{\frac{2}{\omega\mu\sigma}} \tag{4.19}$$

For conductivities greater than 30 S/m the difference between δ_g and δ_c is less than 1%, validating the simplified form for the conductivities of interest. The graphite materials were also shown to satisfy the criteria for a good conductor in the section 3.3. Figure 4.2 shows a cross section view of a plane wave impinging on a conductor's surface.

As the frequency of the EM wave grows larger, the depth into which the wave penetrates into the conductor gets smaller. For high frequencies the electric field and thus the current only occupy a shallow region around the surface of the conductor. This effectively decreases the cross-sectional area of the conductor through which the current can flow, resulting in a higher resistance. Figure A.1, Appendix A shows the skin depth

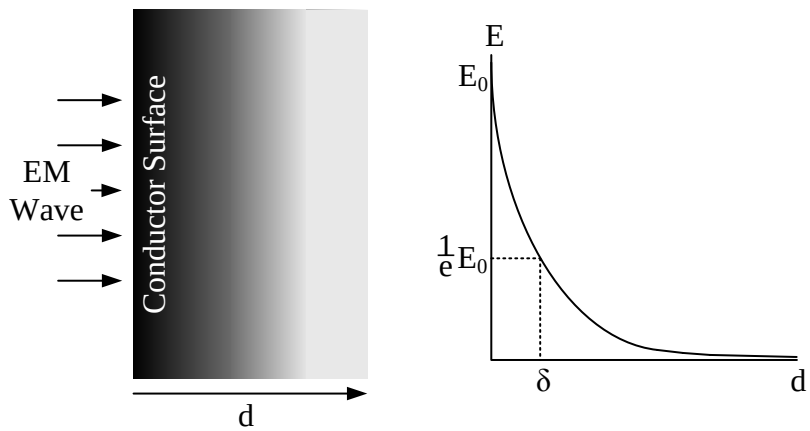

Figure 4.2: Electric field strength in a conductor as a function of depth.

for paper conductivities ranging from 1 to 100,000 S/m at a frequency of 915 MHz. The value of permeability used was the nominal value for pure graphite ($\varepsilon_r = 12$).

For metals, the skin depths are very shallow and increasing the conductor's thickness provides negligible efficiency improvements as the effective cross sectional area of the conductor is only slightly increased. However, for the current graphite paper conductivities of 600 and 39,000 S/m the skin depths are 680 and 84 µm, respectively. These distances are much larger or on par with thickness of the conductive layers, which are 100 µm thick, meaning that a significant amount of current flows in the centre of the conductors. The thickness of the conductive layer thus plays a major factor in the overall loss resistance and radiation efficiency of the antenna. This phenomenon is observed and discussed further in the section 4.6.

The simulation model was set up to evaluate the fields through the entire conductor, with around twenty mesh cells per overall conductor thickness. This is in contrast to using a lossy metal or perfect electrical conductor (PEC) type, which use a one dimensional surface impedance model. Simulation of the entire conductor volume

resulted in significantly longer simulation times but was necessary to achieve accurate results.

4.3 Simulation Setup

With all the information covered in the preceding sections, a model was created in CST Microwave Studio 2015 to aid with the optimization of the RFID antenna. A planar half-wave dipole was used as the foundation for the design as this is by far the most common antenna topology for passive UHF RFID antennas. The dipole antenna is used for its highly omnidirectional radiation pattern in the plane perpendicular to the antenna, relatively simple tuning, and wealth of theoretical and qualitative background knowledge of the structure [7, 30].

A resonant dipole's overall length is approximately given by half the free-space wavelength (λ) of the frequency of interest. For the 915 MHz center frequency of UHF RFID this overall length was about 164 mm. The width of the dipole was arbitrarily chosen to be 10 mm and the gap distance 1 mm, simply as a starting point for the design. The thickness was set to 100 µm, given by the physical materials under investigation.

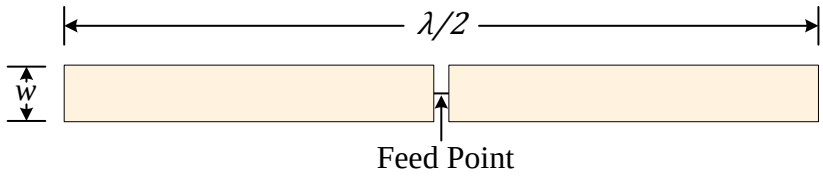

Figure 4.3: Half-wave dipole antenna dimensions.

A half-wave (λ/2) dipole with these dimensions was simulated and fabricated for each of three conducting materials: copper, graphite ink, and exfoliated graphite. The input impedances of the physical antenna were measured to determine if the simulation

models of the antennas were valid. The measurements were performed using an Agilent PNA-X N5242A network analyzer in balanced (differential scattering parameter) mode. A double single-ended to balanced probe was built based on the work done by Palmer and Rooyen to allow accurate measurements of the balance dipole structure using two unbalanced coaxial cables fed into the network analyzer [31].

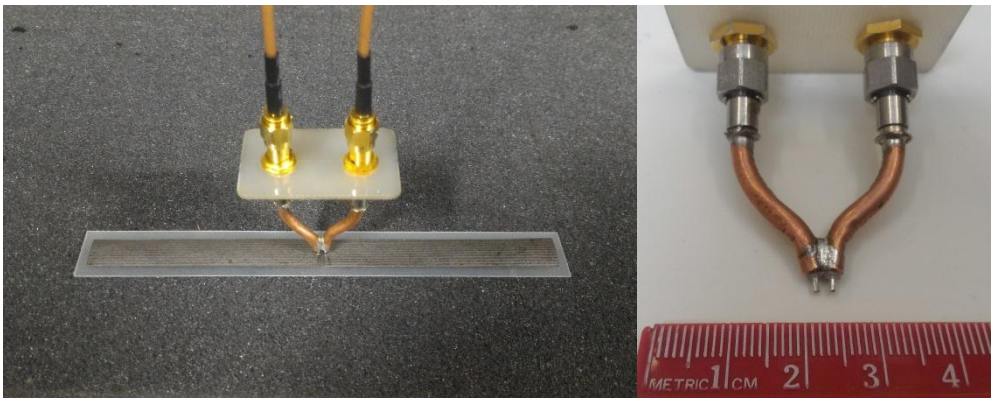

Figure 4.4: Balanced probe measurement setup.

Figure 4.5 shows that there is fairly close agreement between the measured and simulated antenna input impedances for all but the reactive component of the graphite-ink antenna. The measured values reactive component of the impedance was about 30 to 50 Ω lower than the simulated values, however a similar overall shape is still observed. This difference may be explained by a number of factors: Assumptions about the graphite material's permittivity, limitations in mesh cell size, conductivity discrepancies between samples, permittivity discrepancies between substrates, simplifications in the sample thickness due to the presence of elevated ridges, construction variances, network analyzer calibration, and the physical presence of the probe and foam support in the near field of the antenna. An effort was made to reduce the impact of each of these error sources, however they will always be present to some degree.

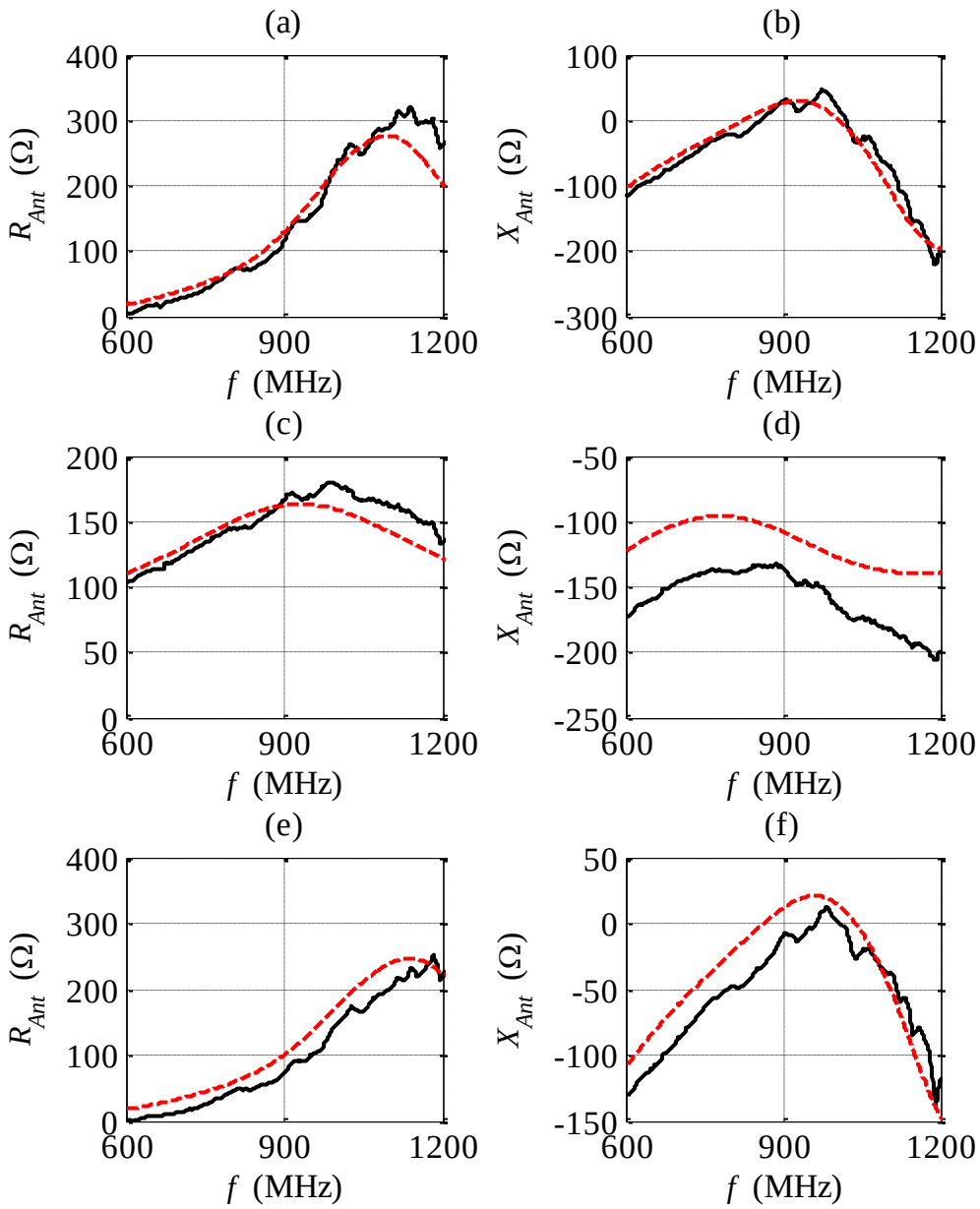

Figure 4.5: Measured and simulated input impedances for copper (a-b), graphite-ink (c-d), and exfoliated-graphite (e-f) half-wave dipoles. Solid: measurement, dashed: simulation.

The simulation model and experimental results thus agree well for the higher conductivities of copper (6×10^7 S/m) and exfoliated graphite (3.9×10^4 S/m), while being less reliable for the lower conductivity of the ink-based graphite (600 S/m). One can thus expect some differences in the behavior of the analytically optimized antennas versus their physical counterparts.

4.4 Dipole Optimization

The first optimization procedure to be made was altering the width and length of the dipole arms to maximize performance. The performance was measured using the equation for the maximum read range derived in the previous Power Optimization section. The read range was generalized for an isotropic transmitting antenna $G_{Tx}(\theta, \phi) = 1$ radiating the maximum allowed power of 4 watts effective isotropically radiated power (EIRP) as regulated by Industry Canada (RSS-247) [32]. EIRP is a metric used to regulate the power density radiated by an antenna in the direction of maximum radiation, and is given relative to an isotropic radiator. It can be found by multiplying the power entering the antenna by its gain.

The optimization process of the dipole antenna was performed using the results of the CST MWS simulations and MatLab algorithms to solve Equation (4.17). An array sweep of all lengths for all widths would provide the best insight into the performance of the antennas, however the simulation times would be prohibitively long. Instead, the process was broken down into the following steps:

1. *The width of the antenna was varied over a set range while the length was held constant at half a wavelength. The width that resulted in the maximum read range was identified.*
2. *The length of the antenna was varied over a set range while the width was set to the value found in step 1.*

The read range was optimized for the centre frequency of interest (915 MHz, both mean and geometric mean) unless the bandwidth of that antenna was particularly narrow over the total operating band (908 – 928 MHz) span. This process was repeated for both graphite-ink and exfoliated-graphite materials. If a maximum read range value could not be found, steps 1 and 2 were repeated with different ranges until one was, or stopped if the values were deemed non-convergent.

4.4.1 Graphite-Ink Dipole

The width of the graphite-ink dipole was varied while the length was held at a constant 164 mm (approximately half a wavelength). Figure 4.6 shows the theoretical read range for each antenna width plotted over the entire UHF RFID operating frequency band. One can see that the read range continuously increases until it reaches its maximum value of 3.37 m, which occurs when the width is the highest (14 mm) in the simulation range. This is not unexpected, and becomes more apparent when the width is considered in relation to the loss resistance of the antenna. As discussed in section 4.2, for relatively low conductivities the current penetrates deep into the centre of the conductor. As the antenna width increases so too does the cross-sectional area of the antenna element, effectively lowering the resistance to the current that flows through it. The loss resistance is a

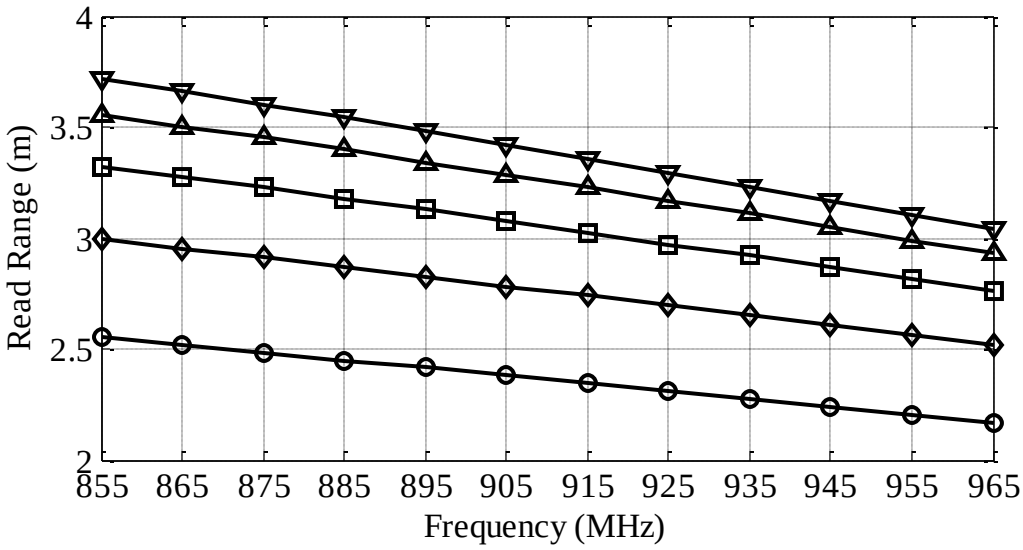

Figure 4.6: Simulated read ranges for 164 mm long graphite-ink dipoles of various widths. ○: w = 6 mm, ◇: w = 8 mm, □: w = 10 mm, △: w = 12 mm, ▽: w = 14 mm.

measure of the energy lost to these ohmic (heat) losses, and as such one would expect it to decrease for increasing widths. This behavior is verified by observing the changes in the radiation efficiency and input resistance, Equation (4.5), both of which are influenced by the loss resistance. Both of these relationships are confirmed in Figure A.2 and Figure A.3, Appendix A. It is apparent that to maximize performance of the graphite-ink dipole the width must be made as large as possible to minimize the loss resistance. The antenna footprint size is an important factor in RFID tag design and must also be taken into consideration. For this reason the author has identified 10 mm as the maximum practical width for the dipole antenna. For applications where the footprint size is not of concern, a width of 14 mm or larger may be used, although an upper bound was not determined.

The next optimization step was to vary the length of the graphite-ink dipole with a constant 10 mm width as previously identified. Figure 4.7 shows the theoretical read

range for each antenna, concentrated around the frequency band of interest for clarity. A plot with the full frequency span can be found in Figure A.4, Appendix C.

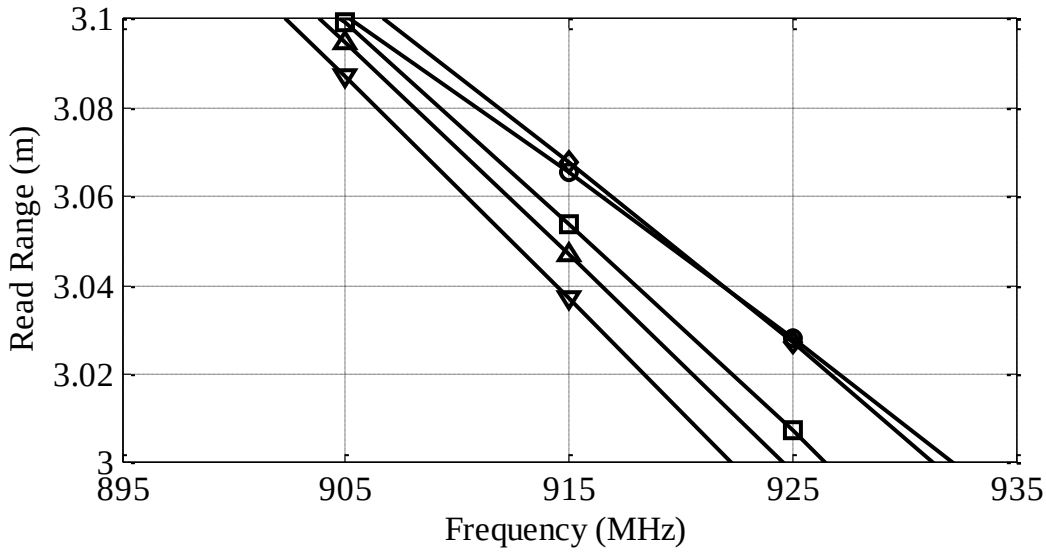

Figure 4.7: Simulated read ranges for 10 mm wide graphite-ink dipoles of various lengths. ○: l = 149 mm, ◇: l = 152 mm, □: l = 155 mm, △: l = 158 mm, ▽: l = 161 mm.

The differences in read range with changing length are much less pronounced than those related to width variations. This is likely explained by the relatively small length changes and the smaller impact the length has on the loss resistance compared to that of the width. Changing the length has no impact on the cross-sectional area of the antenna element, as it simply adds a few millimetres of resistive material to the ends of the antenna which can radiate and dissipate power. Although the changes in read range are marginal, it is nevertheless maximized at an overall antenna length of 152 mm for a read range of 3.07 m. The overall dimensions and antenna characteristics are summarized in Table 4.1.

Further simulations of varying dipole lengths (Figure A.5, Appendix A) show that a read range that falls within 99% of the maximum can be achieved when l = 143 mm,

and within 95% when l = 131 mm. Although these are not the best performing antennas in terms of absolute read range, they have a smaller footprint and reduce the manufacturer's material costs and while sacrificing minimal performance.

4.4.2 Exfoliated-graphite Dipole

The optimization process was repeated for the exfoliated-graphite material using the same procedures as before. The simulation model remained largely the same, only a change in the conductivity value of the antenna material was required. The full frequency span plots can be found in Figure A.6 and Figure A.7, Appendix C.

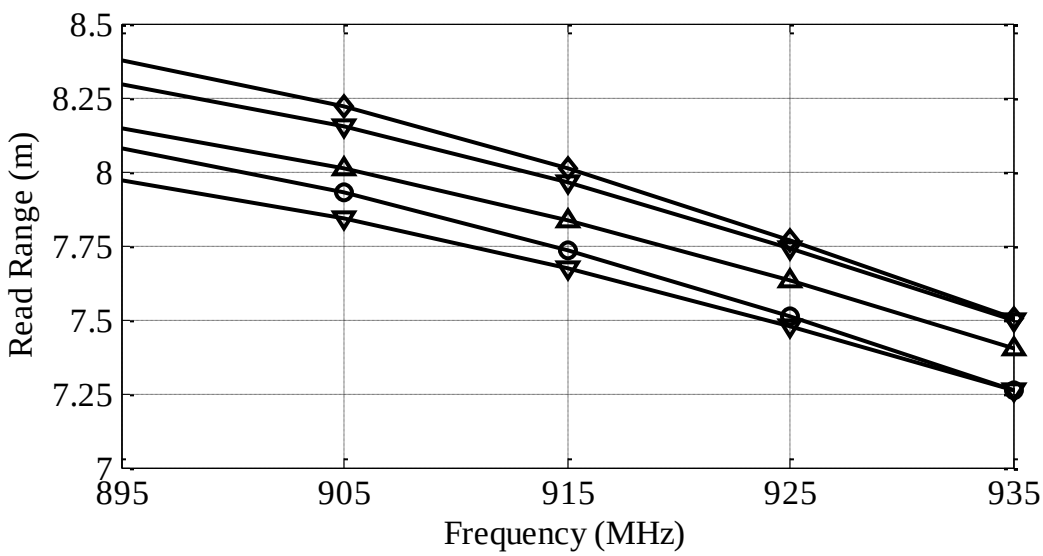

Figure 4.8: Simulated read ranges for 164 mm long exfoliated-graphite dipoles of various widths. ○: w = 1 mm, ◇: w = 3 mm, □: w = 5 mm, △: w = 7 mm, ▽: w = 9 mm.

Comparison of Figure 4.8 and Figure 4.9 shows much larger read ranges are achievable for the exfoliated-graphite material than the graphite ink. In Figure 4.8 one can see that the read range is maximized when the width of the dipole element is approximately 3 mm. This behavior is very different than that of the graphite-ink dipole

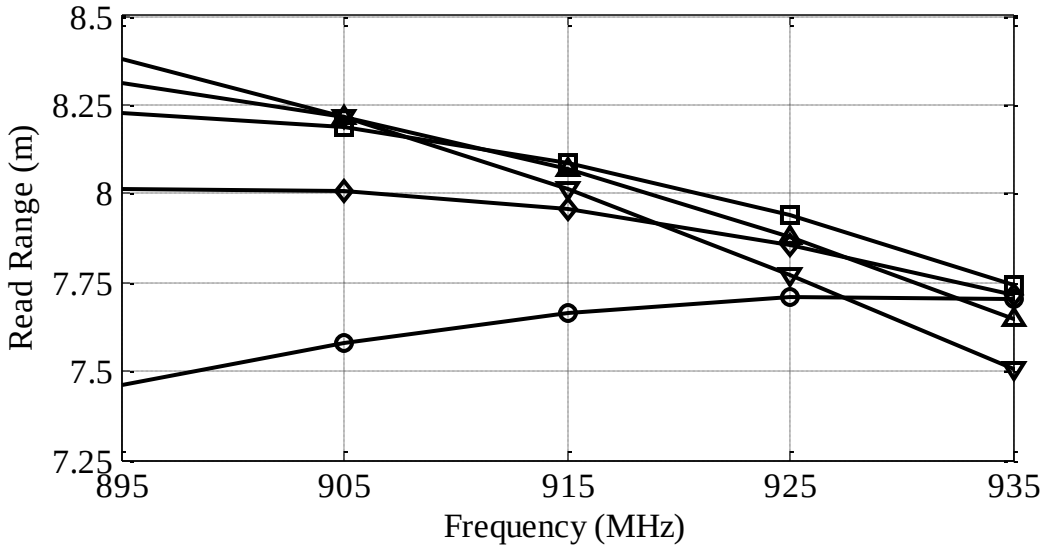

Figure 4.9: Simulated read ranges for 3 mm wide exfoliated-graphite dipoles of various lengths. ○: l = 152 mm, ◇: l = 155 mm, □: l = 158 mm, △: l = 161 mm, ▽: l = 164 mm.

where the read range continued to increase as the width was increased. This suggests that the exfoliated-graphite material is conductive enough to reduce the impact of the loss resistance on the radiation performance of the antenna. The radiation resistance, which is heavily determined by the current distribution (a function of the antenna geometry), is no longer dominated by the ohmic losses in the antenna and thus largely determines the input impedance of the antenna. Comparing the radiation efficiencies of the exfoliated-graphite (Figure A.8, Appendix A) and graphite-ink antennas shows much higher efficiencies for the former. The relationship between radiation efficiency, loss resistance, and radiation resistance, Equation (4.5), agrees with the previous comments, and shows that the radiation resistance dominates the loss resistance at the higher conductivity.

The read range is maximized for a width of 3 mm, although widths of 2 and 4 mm (Figure A.10, Appendix A) give read ranges within 99.9% of this value. From Figure 4.9 one can see that the maximum read range for a 3 mm wide dipole occurs when its length

is approximately 158 mm. The overall dimensions of the optimized antennas are given in Table 4.1. The separation gap was varied without any appreciable effect on the results.

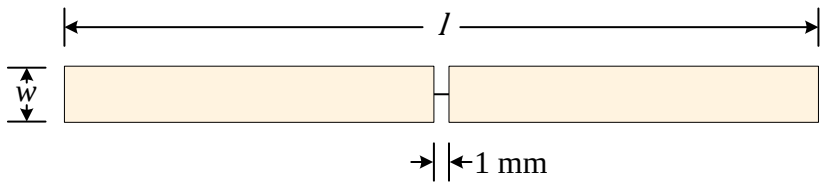

Figure 4.10: Optimized dipole antenna configuration.

Table 4.1: Optimized dipole antenna dimensions.

Graphite-ink Antenna		Exfoliated-graphite Antenna	
Length *l* (mm)	Width *w* (mm)	Length *l* (mm)	Width *w* (mm)
152	10	158	3

The maximum theoretical read ranges for the optimized antennas were 3.07 and 8.09 m for the graphite-ink and exfoliated-graphite antennas respectively.

The directivities were measured for both graphite based antennas and were found to be approximately +2.3 dBi in both cases. This agrees with the findings in [18], which state that the directivities of the half-wave dipoles are relatively constant for the conductivities of interest ($D_0 \approx +2.2$ dBi). This slight discrepancy is likely due to the optimized antenna dimensions being slightly different than those used in Rouse's research.

As the dipole length is increased the directivity becomes more skewed in the [$\theta = 0$] direction, while reducing the length results in a more isotropic directivity. These results both agree with the theoretical predictions in [24]. A more isotropic radiation pattern is generally preferred for most general RFID applications, however the changes are so marginal over the dimensions of interest that they can safely be ignored in favor of

optimizing other important antenna parameters such as radiation efficiency and input impedance.

Depending on manufacturing capabilities the final antenna designs that should be used are given in Table 4.1. These are simple in geometry and can thus be fabricated with relative ease. It is in the author's interest, however, to determine if other matching techniques can be used to further improve the performance of the antennas. These are explored in the following sections.

4.5 T-match

The second optimization technique to be applied to the RFID antenna was the T-matching technique. First described by Uda and Mushiaki, the T-match has become very common in the design of traditional RFID tags and is one of the most prominent impedance matching techniques [33, 34]. Extensive analysis of the T-match can be found in the literature [24, 33, 34] and for brevity will not be covered in this thesis. Only the design steps required to optimize the antenna impedance will be discussed.

The total antenna input impedance is given by the equivalent circuit in Figure 4.11b, which is a combination of the non-radiating transmission line mode impedance Z_t and the radiating antenna mode impedance Z_a. The antenna mode impedance is simply given by the centre-point free space impedance of the dipole without the T-match, identical to what was found in the section 4.4.2. The current division factor α is given for cylindrical conductor shapes and measures how the total current is divided between the upper and lower conductors. It is dependent on the radius of the upper conductor a_1 and the lower conductor a_2 and their separation s_e. Mathematically this is given by [24]

(a)

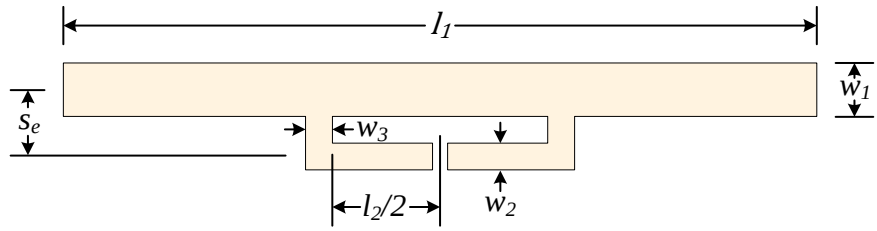

(b)

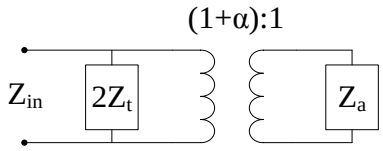

Figure 4.11 T-match dipole antenna dimensions (a) and equivalent circuit (b).

$$\alpha = \frac{\cosh^{-1}\left(\frac{v^3 - u^2 + 1}{2v}\right)}{\cosh^{-1}\left(\frac{v^2 + u^2 - 1}{2uv}\right)} \approx \frac{ln(v)}{ln(v) - ln(u)} \tag{4.20}$$

where

$$u = \frac{a_1}{a_2}, \qquad v = \frac{s_e}{a_2}$$

The transmission line mode impedance can be calculated by treating the T-match as two segments of shorted transmission line, with length $l_2/2$:

$$Z_t = jZ_0 \tan\left(\frac{2\pi}{\lambda}\frac{l_2}{2}\right) \tag{4.21}$$

where

$$Z_0 \approx 276 \log\left(\frac{s_e}{\sqrt{a_1 a_2}}\right) \tag{4.22}$$

The total input impedance given in Figure 4.11 (b) can be written as

$$Z_T = \frac{2Z_t(1+\alpha)^2 Z_a}{2Z_t + (1+\alpha)^2 Z_a} \tag{4.23}$$

Equation (4.23) is defined for an antenna of cylindrical conductors, while the dipoles under consideration are planar. For very thin planar conductors an equivalent cylindrical radius can be computed and is given by [24]

$$a_e = \frac{1}{4} w_p \tag{4.24}$$

where w_p is the width of the planar strip. Substituting this equivalent radius into Equations (4.20), (4.21), and (4.22) yields

$$\alpha = \frac{ln\left(\frac{4s_e}{w_2}\right)}{ln\left(\frac{4s_e}{w_2}\right) - ln\left(\frac{w_1}{w_2}\right)} \tag{4.25}$$

$$Z_0 \approx 276 \log\left(\frac{4s_e}{\sqrt{w_1 w_2}}\right) \tag{4.26}$$

$$Z_t = jZ_0 \tan\left(\frac{2\pi}{\lambda} \frac{l_2 + w_3}{2}\right) \tag{4.27}$$

These three equations along with Equation (4.23) characterize the total input impedance based on the geometry described in Figure 4.11a. Setting a_1 equal to a_2 sets α to unity, reducing Equation (4.23) to

$$Z_t = \frac{8Z_t Z_a}{2Z_t + 4Z_a} \tag{4.28}$$

Reich and Bauer-Reich showed that this T-match analysis predicts accurate results for planar antennas that satisfy the geometric ranges given in Table 4.2 [34].

A T-match configuration was simulated for each of the optimized dipole antennas found in the previous section. The parameters described in Table 4.2 could not be satisfied for the graphite antenna since the width of the antenna elements (10 mm) did not

Table 4.2: Valid geometric ranges for analytical T-match expressions given by Reich and Bauer-Reich [34].

Parameter	Valid Range	Valid Range at 915 MHz
l_2	$\leq 0.06\lambda$	$\leq$ 19.7 mm
s_e	$\leq 0.009\lambda$	$\leq$ 2.95 mm
α	≈ 1	≈ 1

allow for the corresponding antenna dimensions without overlapping conductors. Nevertheless, a T-match sweep of l_2 was performed using a uniform element width (w_1, w_2, and w_3) of 10 mm, with s_e = 11, resulting in a 1 mm spacing between the top and bottom elements.

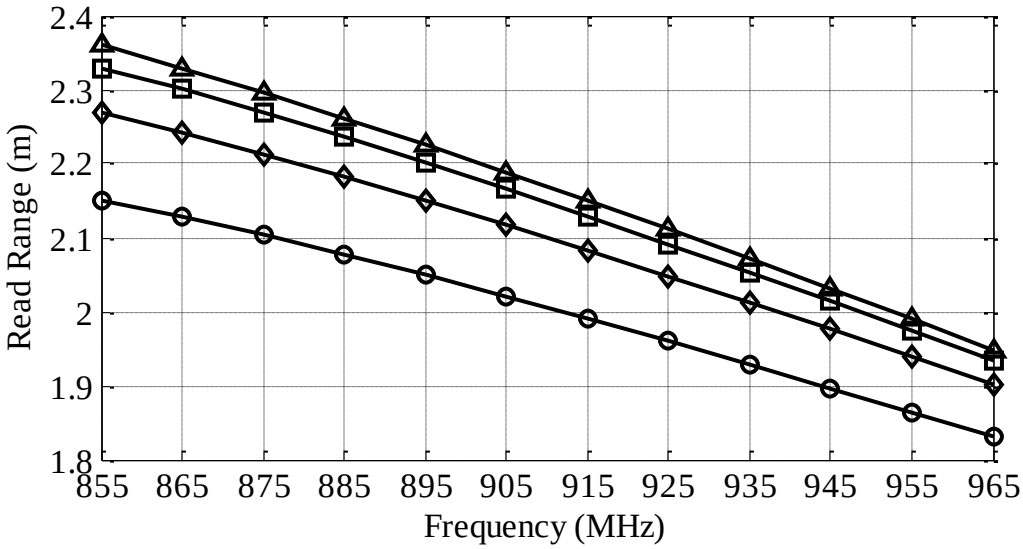

Figure 4.12: Simulated read ranges for graphite-ink T-match dipoles for various lengths of l_2 and s_e = 11. ○: l_2 = 30 mm, ◇: l_2 = 40 mm, □: l_2 = 50 mm, △: l_2 = 60 mm.

Comparing Figure 4.12 to the read range of the optimized dipole one can see a significant reduction with the introduction of the T-match. This is almost certainly due to

the large increase in loss resistance when the bottom antenna element is added, which is reflected in the very low radiation efficiency of the antenna (Figure A.11, Appendix C). The use of a T-match can thus provide no benefit to the performance of the graphite-ink based tag antenna.

A T-match configuration was simulated for the exfoliated-graphite material for a uniform element width (w_1, w_2, and w_3) of 3 mm and s_e = 5 and 7, corresponding to a 2 mm and 4 mm spacing between the top and bottom elements respectively.

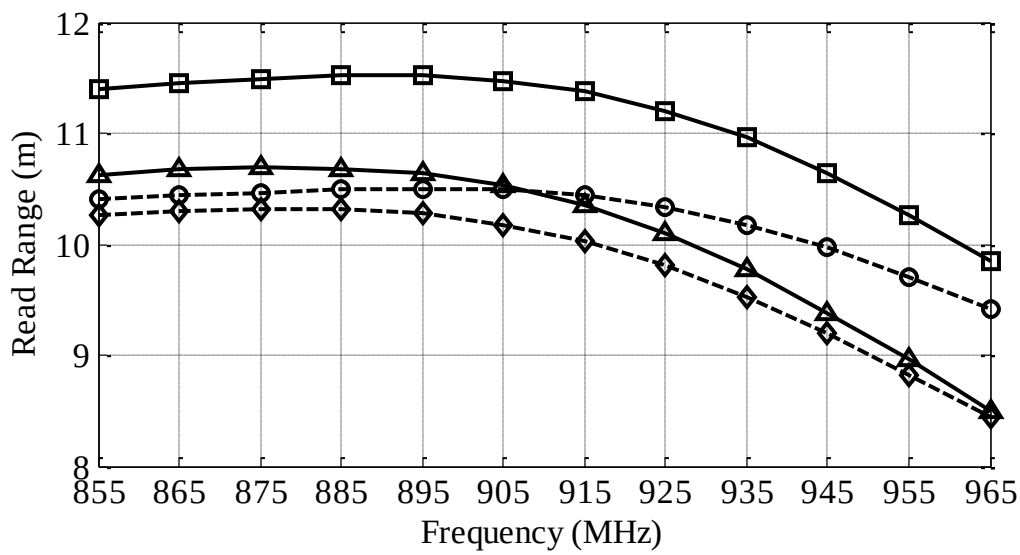

Figure 4.13: Simulated read ranges for exfoliated-graphite T-match dipoles with various values of l_2 and s_e. ○: l_2 = 50 mm; s_e = 5 mm, ◇: l_2 = 60 mm; s_e = 5 mm, □: l_2 = 40 mm; s_e = 7 mm, △: l_2 = 50 mm; s_e = 7 mm.

Figure 4.13 shows only the combinations of s and l_2 which result in the best read ranges. The complete results can be found in Figure A.12 and Figure A.13, Appendix A. Comparison of Figure 4.13 and the optimized dipole shows a substantial increase in read range for certain combinations of s and l_2. The theoretical read range is maximized when s_e = 7 mm and l_2 = 40 mm to a value of 11.4 m, which is a 41% increase over that of the optimized dipole. Similar to the graphite ink, the exfoliated-graphite T-match antenna has

a lower radiation efficiency than the dipole it was built upon, however the mismatch losses due to the impedance transformation that the T-match provides are reduced enough to provide a net increase in performance.

The results of the simulation are compared with the analytical predictions of Equations (4.26), (4.27), and (4.28) in Figure 4.14. The analytical predictions and the simulated results show close agreement for the lower values of l_2 which are closest to satisfying the bounds given in Table 4.2. This suggests that this set of analytical equations can be used as a quick design guide when trying to select the antenna input impedance. This is helpful when matching to different models of tag ICs that present a different impedance than the Alien Higgs 3, which has been used for this project. A description of the characteristics of many tag IC's available in today's market can be found in Table A.1, Appendix A.

The current splitting factor, α, was varied over a 0.8 to 1.2 range with no appreciable change in input impedance. The optimized T-match antenna dimensions are given in Table 4.3.

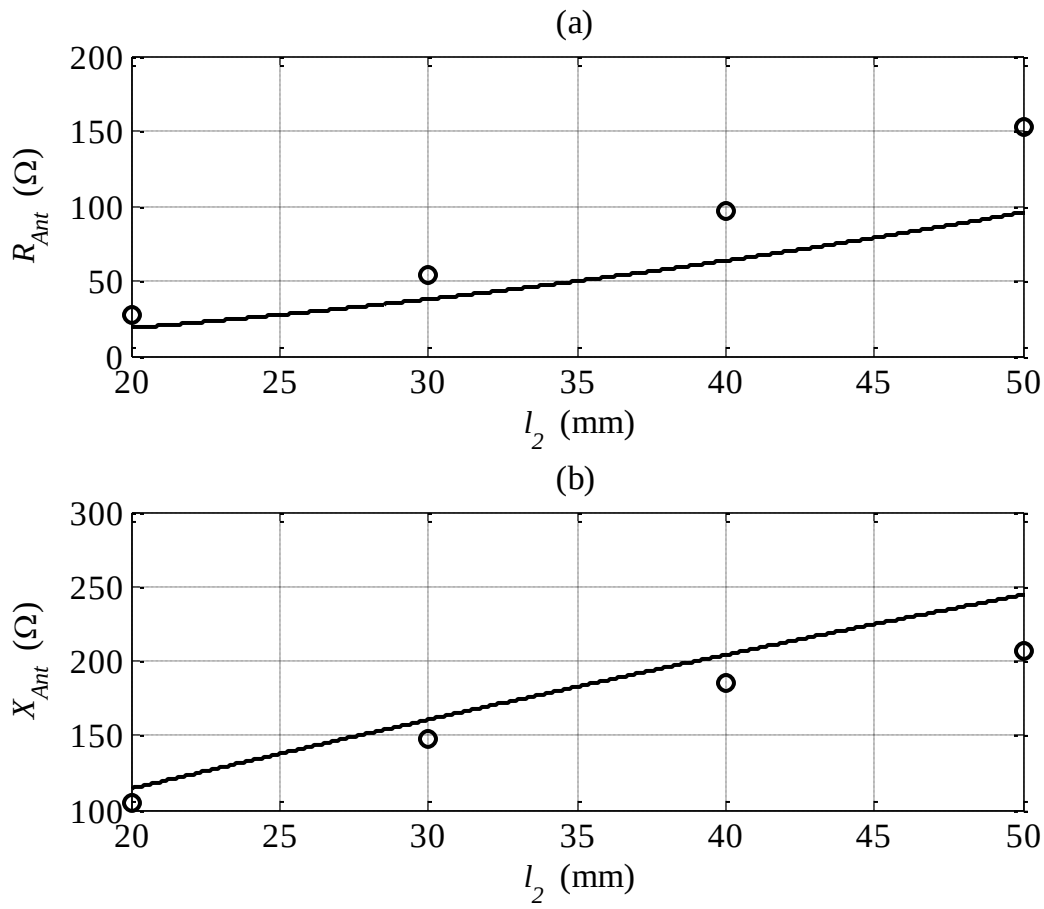

Figure 4.14: Exfoliated-graphite T-match antenna input impedance predicted by analytical equations (solid) and simulations (○) for various lengths of l_2 with s_e = 7.

Table 4.3: Optimized exfoliated-graphite T-match antenna dimensions.

l_1 (mm)	l_2 (mm)	w_1 (mm)	w_2 (mm)	w_3 (mm)	s_e (mm)
158	40	3	3	3	7

4.6 Meander Line Antenna

Meander line antennas (MLA) are an attractive choice for RFID tag antennas as they decrease the overall footprint of the tag antenna. This is achieved by reducing the overall physical length of the antenna while maintaining a sufficient electrical length by folding

the radiators into a zigzag. As a compromise, MLAs generally provide less gain and have a narrower bandwidth than a tuned dipole [35]. The MLA can be completely described by the dimensions given in Figure 4.15. The poor performance of the graphite-ink dipole at widths less than 10 mm prohibited the application of meanders as the final structure would simply be too large and fall outside the allowable footprint. The exfoliated-graphite dipole antenna, however, at a width of 3 mm, provided a good candidate for testing.

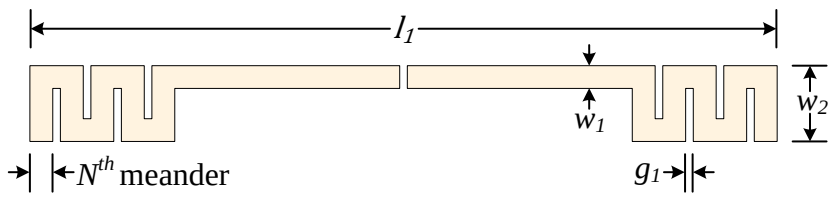

Figure 4.15: Meander Line Antenna dimensions.

The effective length, measured by tracing out the path the current takes along the entire structure, depends on the number of meanders and was chosen to be 164 mm which corresponded to half a wavelength at the center of the frequency band (915 MHz). To fully utilize the allowable area the total width of the antenna was set to 10 mm, and the meander spacing 1 mm. The meanders were pushed to the end of the elements where the current is the lowest, to minimize their impact on the antenna gain. The length of the straight element was set to 60 mm to allow for the addition of a T-match element for further optimization, and the rest of the antenna length was meandered. This resulted in five meanders per element similar to what is shown in Figure 4.15.

The resulting read range can be found in Figure A.14, Appendix A and has a value of 3.57 m at the centre of the frequency band. This is a 56% reduction in read range when compared to the optimized dipole's 8.09 m, however, the overall length of the

antenna has been reduced by 38% to 98 mm from 158 mm. The input impedance of the MLA remained highly capacitive, so further modification of the antenna was performed by the addition of a T-match.

4.7 Meander Line T-match Antenna

The meander line antenna in the previous section was purposely designed to leave enough spacing for the addition of a T-match. The combined structures and their corresponding dimensions are shown in Figure 4.16.

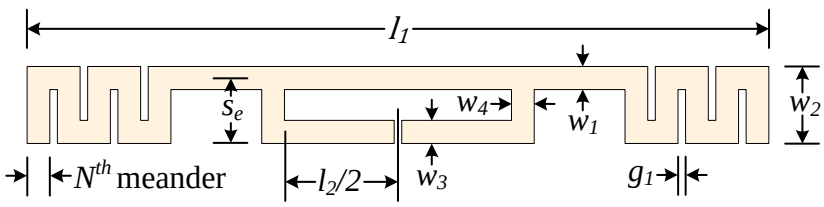

Figure 4.16: T-match meander line antenna dimensions.

A sweep of the T-match length l_2 was performed with a uniform element width (w_1, w_2, and w_3) of 3 mm and s_e = 7 (the same dimensions as the optimized simple T-match).

Figure 4.17 shows that the addition of a T-match element increases the maximum read range of the MLA substantially, up to value of 8.52 m for a T-match length l_2 of 30 mm with good bandwidth. The improved performance is due to the improved impedance match, similar to the T-match antenna based on the simple dipole. A range increase of 5.3% over the optimized dipole was achieved with a 38% shorter antenna length.

A second meander line T-match antenna was simulated using the excess horizontal antenna traces outside the T-match to add an additional meander to each

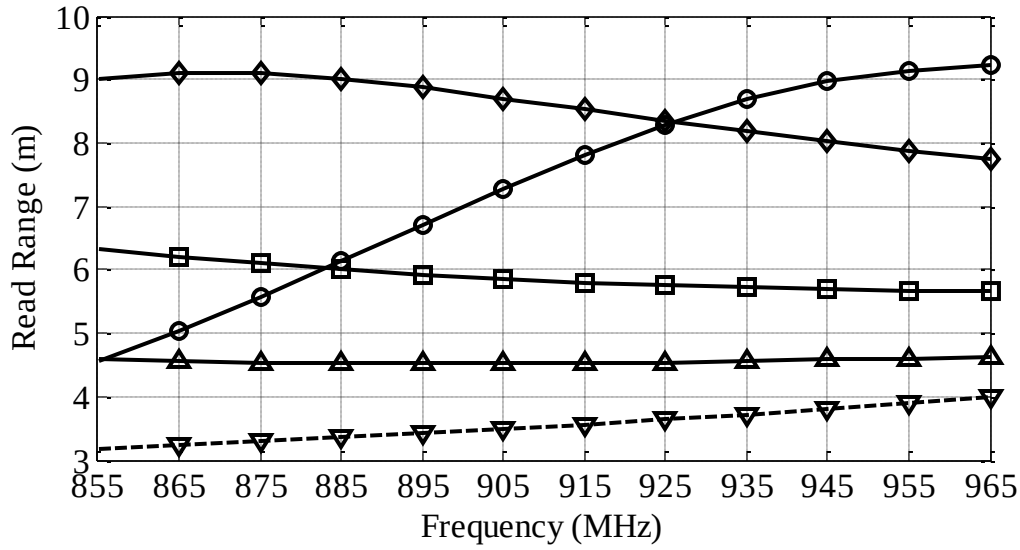

Figure 4.17: Simulated read ranges for exfoliated-graphite MLA with a T-match for various lengths of l_2 with s_e = 7 and N = 5. ○: l_2 = 20 mm, ◇: l_2 = 30 mm, □: l_2 = 40 mm, △: l_2 = 50 mm, ▽: No T-match.

element (N = 6). The trace dimensions remained the same as the previous antenna, however the total length was reduced to 83 mm. The maximum read range was 6.28 m for a length l_2 of 30 mm (Figure A.15, Appendix A). This corresponded to a 22% reduction in read range, with the benefit of a 47% shorter antenna length.

4.8 Conductivity and Thickness

Results of the graphite-ink dipoles showed that the loss resistance, which is influenced by both the conductivity of the material and the cross-sectional area of the antenna element, had a large impact on the performance of the antennas. To investigate this relationship further, simulations were performed to look at a broad range of conductivities and thicknesses past what are currently achievable to identify a target for better performance. A conductivity sweep was performed on a half-wave dipole (identical dimensions to the

antenna used in section 4.3) with a conductor thickness, *t*, of 100 µm while a thickness sweep of the same antenna was performed with a conductivity of 600 S/m.

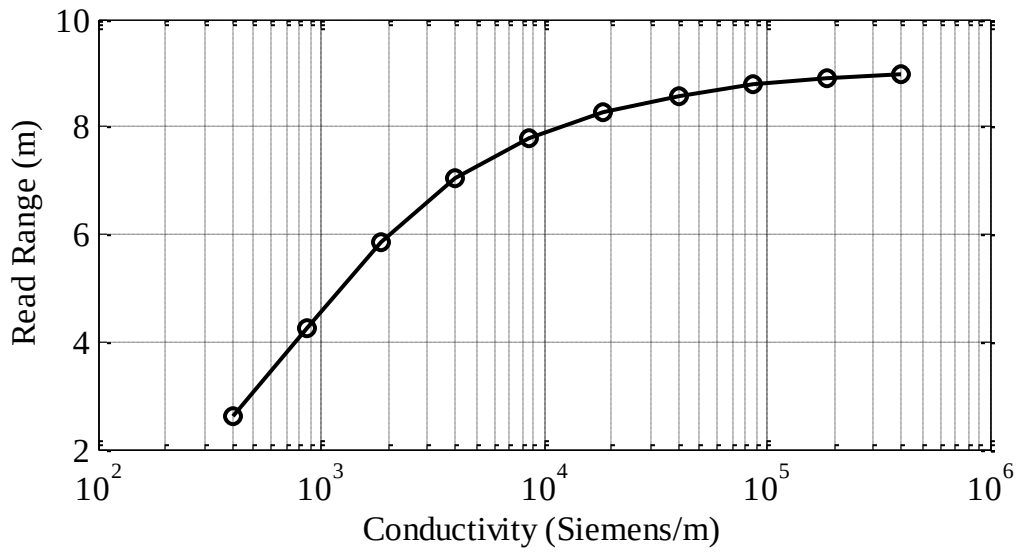

Figure 4.18: Theoretical maximum read range of a half-wave dipole as a function of conductivity.

As the conductivity of the material increases, the loss resistance of the antenna goes down, resulting in higher radiation efficiency and better read range. There are diminishing returns as the conductivity reaches very high numbers however, with marginal improvements past 10^5 S/m. A conductivity of 10^4 S/m appears to be a suitable target for achieving good read range, without being prohibitively high. It is also interesting to note that a doubling of the current graphite paper conductivity from 600 to 1200 S/m results in a 44% increase in read range (3.3 to 4.75 m). Increasing the conductivity from 600 to 1800 S/m results in a read range increase of 74% (3.3 to 5.75m). Higher conductivities may also allow the use of the matching techniques (T-match, meandering) which could not be used for the current incarnation of graphite-ink paper due to excessive resistive losses.

The current paper conductor thickness is limited to 100 µm because of the uncured ink's viscosity and the coating apparatus used to form the paper. Larger thicknesses are potentially achievable using altered ink formulas and coating methods. Figure 4.19 shows the maximum read ranges for a number of thicknesses.

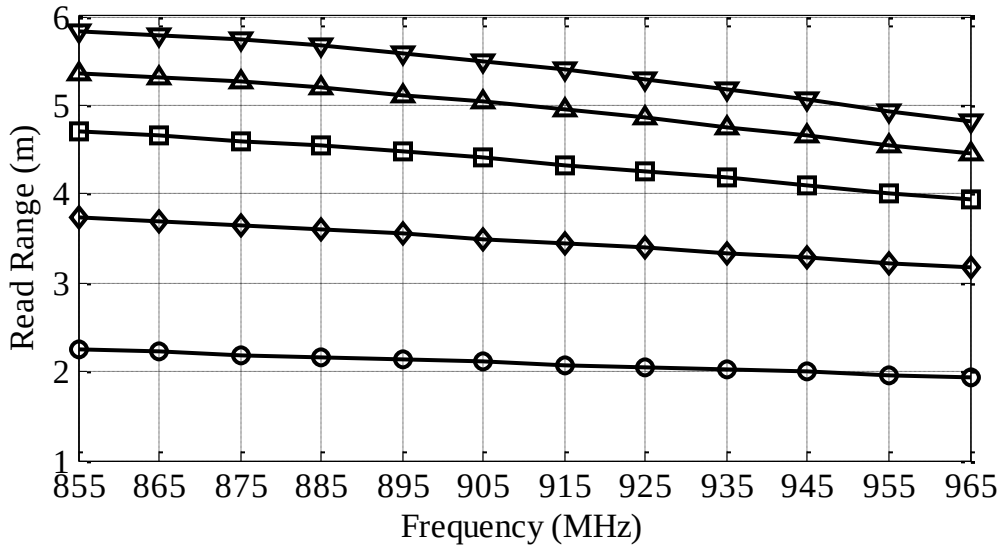

Figure 4.19: Theoretical maximum read range of a half-wave dipole for various thicknesses. ○: t = 50 µm, ◇: t = 100 µm, □: t = 150 µm, △: t = 200 µm, ▽: t = 250 µm.

As expected, the antenna's performance improves as the cross-sectional area of the antenna increases and the loss resistance goes down. Similar to the trend in the conductivity results, there appears to be diminishing returns as the thickness, increases. This is almost certainly due to the thickness approaching the material's skin depth of 680 µm, meaning that further increases in cross sectional area have a marginal effect on the loss resistance. For a doubling of conductor thickness (100 um to 200 um) the maximum read range increased by 44%, about the same performance increase that results from doubling the conductivity. It is apparent that if the conductivity of the graphite-ink

material cannot be improved then using a thicker conductive layer can improve performance as a compromise.

Chapter 5 Antenna Design: Measurements

To validate the simulated antenna designs a physical realization of the structures was necessary. Using graphite-ink and exfoliated-graphite samples fabricated at the Limerick Pulp and Paper Research Centre the optimized antenna designs found in Chapter 4 were built. Their input impedance and maximum read range characteristics were found and compared to their predicted values.

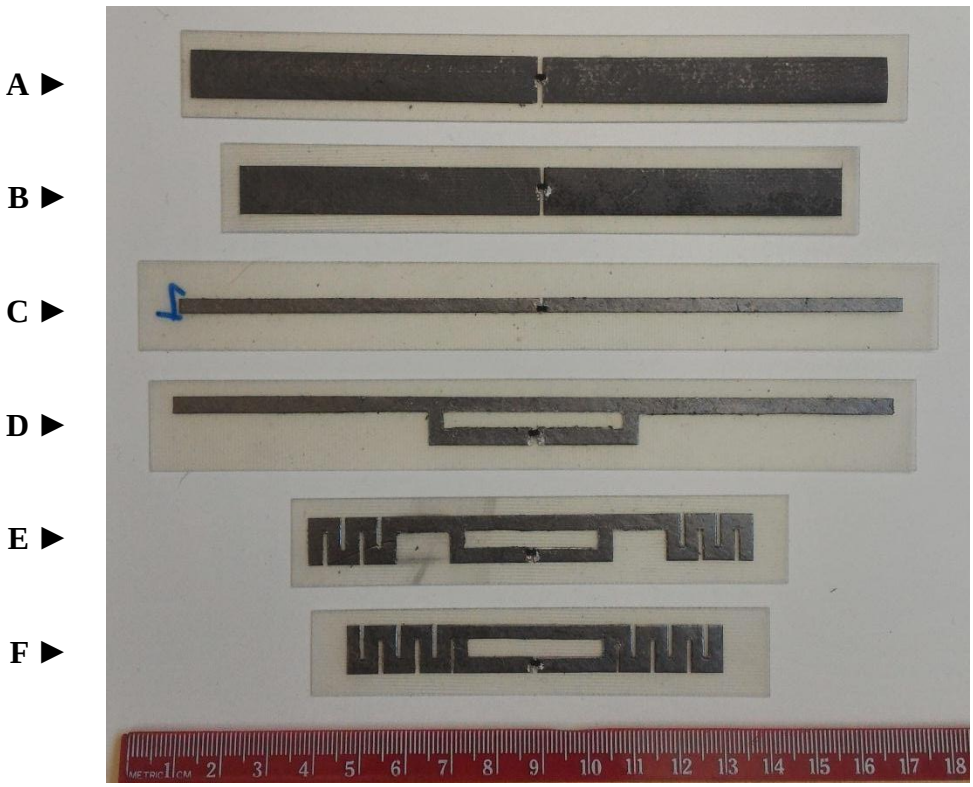

Figure 5.1: Antenna prototypes based on optimized simulations.

The antennas were built by applying a stencil (Appendix B) to the substrate side of the conductive paper and using a guillotine trimmer to cut out the shape of the antenna. The smaller geometric details of the T-match antenna and MLAs were formed using a modeling knife. The paper was then adhered to a sheet of FR4 board for structural

stability using an aerosol adhesive. This structural board was included in all simulations as a lossy dielectric with $\varepsilon_r = 4.5$, $tan\ \delta_c = 0.024$ at 915 MHz and a thickness of 5 mm.

5.1 Input Impedance Measurements

Using the same procedure as described in section 4.3, the input impedances of the six optimized antennas were measured. The extended plots of the input impedances can be found in Figure A.16 – Figure A.18, Appendix A, however the results at the center frequency of 915 MHz are summarized in Table 5.1.

Table 5.1: Simulated and Measured Input Impedances at 915 MHz.

Antenna Type	Simulated Input Impedances (Ω)	Measured Input Impedances (Ω)
A: Graphite-ink Dipole (152 mm)	143.6 - j109.2	186.3 - j137.9
B: Graphite-ink Dipole (131 mm)	123.7 - j85.6	136.5 - j145.7
C: Exfoliated-graphite Dipole (158 mm)	176.4 + j24.5	131.7 + j45.9
D: Exfoliated-graphite Dipole w/ T-Match	96.2 + j184.9	148.2 + j114.8
E: Exfoliated-graphite Dipole w/ T-Match and *N*=5 Meanders	92.4 + j250.7	170.2 + j235.8
F: Exfoliated-graphite Dipole w/ T-Match and *N*=6 Meanders	49.5 + j242.5	135.2 + j241.8

The measured input impedances of the antennas show a similar shape to those of the simulations, however, in nearly all cases the real part of the impedance was higher

than predicted. As discussed in section 4.3 there are a number of factors that may contribute to this discrepancy, the most likely being the varying nature of the graphite-based papers' conductivity between samples, potentially contributing to a higher loss resistance and thus a larger real component to the input impedance. Assumptions about the graphite material's permittivity described in section 3.3 may also lead to differences in the antennas' current distributions and thus their input impedances.

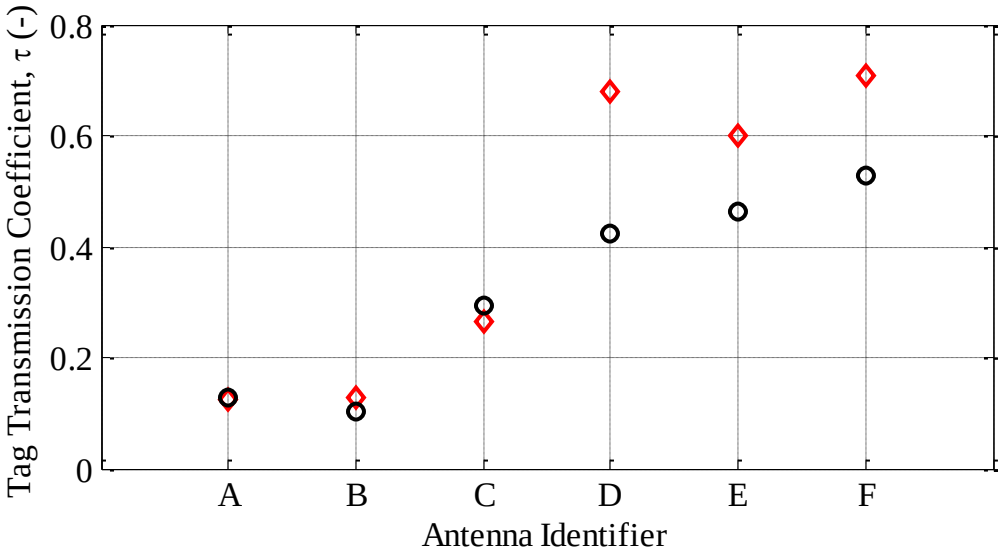

Figure 5.2: Measured and simulated tag transmission coefficients for the six optimized antennas. Antenna identifiers are given in Table 5.1. ○: measurement, ◇: simulation.

The predominant impact of the input impedance on the performance of the RFID system is due to its effect on the tag-antenna transmission coefficient, τ, given by Equation (2.2). A comparison of the simulated and measured transmission coefficients at the centre frequency (915MHz) can be found in Figure 5.2. For antennas A-C (identifiers given in Figure 5.1 and Table 5.1), which are purely dipoles with no matching structures, the measured transmission coefficients are very close to the predicted values. For the antennas D-F, which have more complex geometries, the measured transmission

coefficients are lower than their simulated values, indicating higher mismatch losses than predicted.

5.2 Read Range Measurements

After the input impedances were measured the Alien Higgs 3 (SOT-323 package) IC chips were affixed to the conductive paper antennas using silver conductive epoxy (MG Chemicals 8330S-21G). The test setup (Figure 5.3) used to measure read ranges was a Skyetek SkyeModule M9 RFID reader connected through USB to a PC running the Skyeware 4 application software. The transmitting antenna and tag were placed inside an anechoic chamber to reduce multipath and interference effects. The Skyeware 4 software was used to identify when a tag was visible to the reader, as well as selecting the frequency band (North America) and output power of the reader itself. The read ranges were measured using two different methods: fixed power, variable distance and fixed distance, variable power.

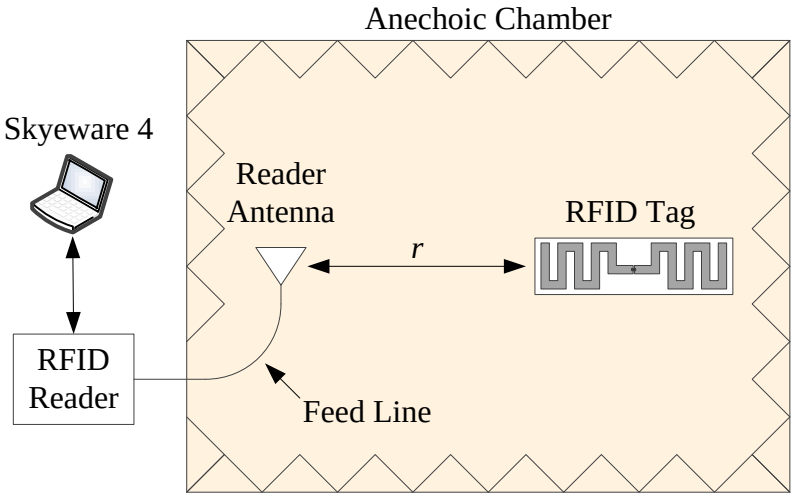

Figure 5.3: Read range measurement test setup.

The fixed power, variable distance method of measuring read ranges is straightforward, and involves setting the output power of the reader to a known value and increasing the distance between the tag and reader until the tag is no longer readable. This method has the difficulty of keeping all the antennas at the same viewing angle to the reader, which will cause variations in the transmitter antenna gain (gain is a function of θ and ϕ, as discussed in Chapter 4). To circumvent this limitation, a fixed distance scheme is also used and compared.

A fixed distance method allows the antennas to be placed in the same location for every reading relative to the transmitting (reader) antenna. This effectively eliminates the variability of the transmitting antenna gain, which is not constant over its viewing angle. The distance between the reader and the tag was set to 1 metre so the antennas (reader and tag) were both located in each other's far-field. The power was varied using the Skyeware 4 software and the minimum power for a successful read was recorded. Using the expression for read range, Equation (4.17), the equivalent maximum read range with full reader output power was calculated so the read ranges could be compared between the two aforementioned methods.

The maximum output power of the M9 reader (0.5 watts = +27 dBm) was used for the fixed power measurements resulting in an EIRP of 1.49 watts when used with the 6.5 dBi reader antenna and factoring in feed line and impedance mismatch losses. Proper polarization alignment was maintained for all measurements. Again, the antenna identifiers are given in Figure 5.1 and the left hand column of Table 5.1.

Comparison of the measured and equivalent read ranges using 1.49 W EIRP in Table 5.2 shows that the methods agree rather closely, with both values for each antenna

Table 5.2: Measured RFID tag read ranges.

Antenna Identifier	Fixed Power, Variable Distance	Fixed Distance, Variable Power	
	Maximum Range at 1.49 W EIRP (m)	Minimum Output Power (dBm)	Equivalent Maximum Range (m)
A	1.40	24.2	1.38
B	1.12	26.4	1.07
C	3.37	15.5	3.67
D	4.05	15.4	4.16
E	1.98	21.3	1.93
F	1.03	26.3	1.08

falling within 10% of each other. The fixed distance, variable power method is therefore a very convenient way to determine maximum read ranges without needing a large physical space, or cumbersome movement of the RFID tag.

Comparison of the simulated read ranges to the measured read ranges required the consideration of the differences between the theoretical and test setup pictured in Figure 5.3. The limited output power of the M9 reader, non-unity transmission coefficient between the feed line and the transmitting antenna, discrepancies in the reported values of the threshold power of the IC chip, and power loss in the feed line were identified as potential differences between the two. Adding these loss factors into the theoretical read range expressions yields the following.

$$r_{Norm} = \frac{\lambda}{4\pi}\sqrt{\frac{G_{Tx}(\theta,\phi)G_{Tag}(\theta,\phi)\tau P_{Tx}C_{Power}\tau_{Tx}L_{Cable}}{C_{Th}P_{Th}}} \tag{5.1}$$

$$r_{Norm} = \underbrace{\sqrt{\frac{L_{Cable}\tau_{Tx}C_{Power}}{C_{Th}}}}_{\substack{Normalization \\ Factor}} \underbrace{\frac{\lambda}{4\pi}\sqrt{\frac{G_{Tx}(\theta,\phi)G_{Tag}(\theta,\phi)\tau P_{Tx}}{P_{Th}}}}_{\substack{Theoretical\ Read\ Range \\ Expression}} \tag{5.2}$$

$$r_{Norm} = \underbrace{\sqrt{\frac{L_{Cable}\tau_{Tx}C_{Power}}{C_{Th}}}}_{\substack{Normalization \\ Factor}} r_{Max} \tag{5.3}$$

where L_{Cable} = 0.676 (-1.7 dB), τ_{Tx} = 0.986, C_{Power} = 0.558, and C_{Th} = 1 to 3.16 (0 to 5 dB). L_{Cable} is the cable loss and τ_{Tx} is the power transmission coefficient between the feed line and the transmitting antenna. C_{Power} represents the difference in EIRP due to the limited 0.5 watt output of the M9 reader, while C_{Th} is the factor that represents the difference in the nominal and experimental values of the threshold power for the Alien Higgs 3 chip. According to [36] the measured threshold power of -13 dBm for the Higgs 3 IC differs significantly from the manufactures specification of -18 dBm, so this range was incorporated into the normalization factor. The total EIRP of the test setup was limited to 1.49 watts, 63% less than the maximum allowed by Industry Canada.

These four terms form a unitless number set which can be multiplied on to the simulated read ranges to give a value that is normalized to the physical test system setup (Figure 5.3). The normalized simulation read ranges are given by vertical bars whose upper and lower bounds are given for a threshold power of -18 and -13 dBm respectively.

Figure 5.4 shows how accurately the simulation models predict the actual read range of the physical antennas. The first four optimized antennas' measured read ranges fall within the bounds of the normalized simulation ranges, and tend towards the lower end. These simulation models therefore predict the true read range fairly well when a

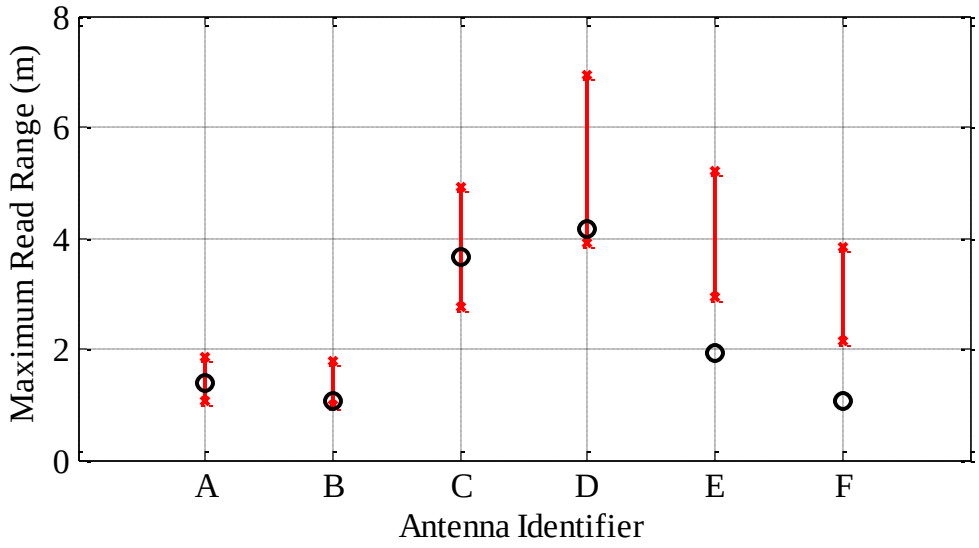

Figure 5.4: Maximum read range for measured antennas and simulated antennas normalized to the physical test setup. O: measurement, ×: simulation.

threshold power closer to the value of -13 dBm reported in [36] is used in the conversion factor.

The results of two graphite-ink based dipoles show that a shorter dipole can be used to reduce the antenna footprint, however the read range penalty (22% shorter) is higher than what was predicted by simulation. The exfoliated-graphite dipole and T-match dipole both performed the best out of all antennas as expected, although improvements in the latter (13% longer range) were not as large as predicted. Nevertheless, for a small increase in antenna complexity a longer read range can be achieved.

Both exfoliated-graphite MLA's perform worse than their simulation counterparts, falling below the normalized range boundary. This may be due to the meshing around the more complex geometry of the antennas. The *N*=5 element MLA has a maximum read distance 54% smaller than the optimized T-match antenna and is 38% shorter, whereas the *N*=6 element MLA has a maximum read distance 74% smaller than the optimized T-

match and is 47% shorter. Despite having lower read ranges than expected, the MLAs were still readable over a metre away using an EIRP of 1.49 W. Using an RFID system with the full allowable power (4W EIRP) increases this range even further which may render them suitable for many applications. The maximum read ranges for all measured antennas using 4 W EIRP are shown in Table 5.3.

Table 5.3: Theoretical read ranges for all measured antennas using 4 W EIRP.

Antenna Type	Maximum Read Range at 1.49 W EIRP (m)	Maximum Theoretical Read Range at 4 W EIRP (m)
A	1.38	2.26
B	1.07	1.75
C	3.67	6.01
D	4.16	6.83
E	1.93	3.16
F	1.08	1.78
Alien Squiglette (ALN-9630)	1.15	1.88

To get an idea of how the six optimized antennas compared to current commercial metal-based products, the read range of an Alien Higgs 3 IC-based tag (Alien Squiglette, ALN-9630) was measured. Using the same anechoic chamber test setup, a read range of 1.15 m was found using an EIRP of 1.49 W, which corresponds to a range of 1.88 m using an EIRP of 4 W. Table 5.3 shows that the graphite-ink tags perform comparably to the ALN-9630, however both are much larger than its 70 mm by 9.5 mm footprint. The short graphite-ink dipole's read range is 6.9% shorter while being 97% larger in area compared to the commercial tag. The exfoliated-graphite antennas which are smallest in

size perform similarly to the ALN-9630. The *N*=6 element MLA's read range is 5.3% shorter while being 23% larger in area. The final selection of any of the antenna designs must ultimately come down to what is acceptable for the application, with size, antenna complexity, and performance all factoring into the choice.

Chapter 6 Conclusion

As item level RFID tagging in supply chain environments becomes more ubiquitous, the motivation to improve tag fabrication methods and environmental impact grows larger. An alternative to the traditional metal-on-PET technology, graphite-based conductors using paper substrates were identified as a potential solution to these issues. Two compounds produced at the Limerick Pulp and Paper Research Centre – graphite-ink and exfoliated-graphite based paper – were characterized and analyzed on their radiation performance.

A microscopic consideration of the electromagnetic interactions of the predominantly carbon structures determined that, at the frequencies of interest, the materials behaved similar to good conductors, and could be subject to the same rules. The conductivities of the graphite-ink-based and exfoliated-graphite materials were found to be approximately 600 and 39,000 S/m, respectively, using both the linear four-point and van der Pauw methods as confirmation.

An expression for the maximum read range of a tag as a function of the total system parameters (gain, threshold and transmit power, antenna and load impedances) was derived and used to determine theoretical read ranges of a number of antenna structures based on simulation models created in CST Microwave Studio 2015. These predictions were compared to anechoic chamber measurements and showed that the two agreed reasonably well and could be used as a guideline to optimize tag antenna structures.

For a 0.5 W output RFID reader with a 6.5 dBi transmitting antenna a maximum read range of 1.38 m was achieved for a tag built using graphite-ink-based paper, and

4.16 m for a tag built using exfoliated-graphite-based paper. These numbers correspond to maximum theoretical read ranges of 2.26 m and 6.83 m respectively for a 4 W EIRP (maximum allowable power in Canada and the United States of America) RFID system.

Six total designs were found with varying levels of performance, complexity, size, and material, and are described in Chapter 4. One-to-one scale stencils of the final designs with their corresponding dimensions are given in Appendix B.

6.1 Future Recommendations

Simulations of the conductivity and thickness of the graphite-ink-based papers showed that developments in these areas could lead to even better tag performance. Should these improvements be made, optimization of the tag antennas with the new paper characteristics would likely yield even better performance and a smaller antenna footprint. A conductivity of 10^4 S/m was identified as a good target before diminishing returns on performance occur.

Improvements to the simulation model and measurement setup may also be an area of interest. Despite showing similar trends, there were still discrepancies found between predicted antenna input impedances and the ones measured. Further fine tuning of the simulation parameters and probe setup may lead to a better correlation between these values and thus improve the performance prediction accuracy of the antenna models. Experimentally determining the permittivity of the graphite papers may also help minimize the errors which arise due assumptions associated with the parameter.

Minimizing simulation times would shorten the optimization process drastically due to the iterative nature of RFID antenna design. This might be accomplished by

developing an appropriate one-dimensional or ohmic-sheet model of the graphite conductors.

Finally, should large production of these graphite-paper based tags begin, a more cost and time-effective alternative to the conductive epoxy used to affix the tag ICs to the antennas should be found. The author has identified anisotropic conductive paste as a potential solution, however others may also be suitable.

Bibliography

[1] K. Finkenzeller, *RFID Handbook: Fundamentals and Applications in Contactless Smart Cards, Radio Frequency Identification*. Chicester, West Sussex, UK: John Wiley & Sons Ltd., 2003.

[2] R. Bansal, "Coming soon to a Wal-Mart near you," *Antennas and Propagation Magazine, IEEE,* vol. 45, pp. 105-106, 2003.

[3] M. Roberti. (2004, December 19). *'Growing' Low-Cost RFID Antennas*. Available: http://www.rfidjournal.com/articles/view?975

[4] R. Das. (2014, October 30). *Passive RFID grows by 1.12 billion tags in 2014 to 6.9 billion*. Available: http://www.idtechex.com/research/articles/passive-rfid-grows-by-1-12-billion-tags-in-2014-to-6-9-billion-00007031.asp

[5] C. J.-P., M. Declercq, C. Dehollain, and N. Joehl, *Design and Optimization of Passive UHF RFID Systems*. New York, New York: Springer Science+Business Media, 2007.

[6] D. Kuester and Z. Popovic, "How Good Is Your Tag?: RFID Backscatter Metrics and Measurements," *Microwave Magazine, IEEE,* vol. 14, pp. 47-55, 2013.

[7] K. V. S. Rao, P. V. Nikitin, and S. F. Lam, "Antenna design for UHF RFID tags: a review and a practical application," *Antennas and Propagation, IEEE Transactions on,* vol. 53, pp. 3870-3876, 2005.

[8] A. Dziedzic and P. Slobodzian, "Electromagnetic properties of materials used for paper printed RFID tag antennas," in *Electromagnetics in Advanced Applications, 2009. ICEAA '09. International Conference on*, Torino, 2009, pp. 760-763.

[9] A. Rida, Y. Li, R. Vyas, and M. M. Tentzeris, "Conductive Inkjet-Printed Antennas on Flexible Low-Cost Paper-Based Substrates for RFID and WSN Applications," *Antennas and Propagation Magazine, IEEE,* vol. 51, pp. 13-23, 2009.

[10] A. Rida, Y. Li, and M. M. Tentzeris, "Design and characterization of novel paper-based inkjet-printed UHF antennas for RFID and sensing applications," in

Antennas and Propagation Society International Symposium, 2007 IEEE, Honolulu, HI, 2007, pp. 2749-2752.

[11] P. V. Nikitin, S. Lam, and K. V. S. Rao, "Low cost silver ink RFID tag antennas," in *Antennas and Propagation Society International Symposium, 2005 IEEE*, Washington, DC, 2005, pp. 353-356 vol. 2B.

[12] W. Pachler, I. Russo, W. Bosch, G. Hofer, G. Holweg, and M. Mischitz, "A silver ink-jet printed UHF booster antenna on flexible substratum with magnetically coupled RFID die on-chip antenna," in *Antennas and Propagation (EuCAP), 2013 7th European Conference on*, Gothenburg, 2013, pp. 1730-1733.

[13] G. Bo and M. M. F. Yuen, "Optimization of silver paste printed passive UHF RFID tags," in *Electronic Packaging Technology & High Density Packaging, 2009. ICEPT-HDP '09. International Conference on*, Beijing, 2009, pp. 512-515.

[14] M. M. Tentzeris, A. Rida, A. Traille, L. Hoseon, V. Lakafosis, and R. Vyas, "Inkjet-printed paper/polymer-based RFID and Wireless Sensor Nodes: The final step to bridge cognitive intelligence, nanotechnology and RF?," in *General Assembly and Scientific Symposium, 2011 XXXth URSI*, Istanbul, 2011, pp. 1-4.

[15] A. Mehdipour, C. W. Trueman, A. R. Sebak, and S. V. Hoa, "Carbon-fiber composite T-match folded bow-tie antenna for RFID applications," in *Antennas and Propagation Society International Symposium, 2009. APSURSI '09. IEEE*, Charleston, SC, 2009, pp. 1-4.

[16] E. Yilmaz, D. P. Kasilingam, and B. M. Notaros, "Performance analysis of wearable microstrip antennas with low-conductivity materials," in *Antennas and Propagation Society International Symposium, 2008. AP-S 2008. IEEE*, San Diego, CA, 2008, pp. 1-4.

[17] A. M. Ferendeci and C. L. H. Devlin, "Microwave characterization of graphite and intercalated graphite as an antenna element," in *Aerospace and Electronics Conference (NAECON), 2012 IEEE National*, Dayton, OH, 2012, pp. 8-10.

[18] C. D. Rouse, M. R. Kurz, B. R. Petersen, and B. G. Colpitts, "Performance Evaluation of Conductive-Paper Dipole Antennas," *Antennas and Propagation, IEEE Transactions on,* vol. 61, pp. 1427-1430, 2013.

[19] B. Huang, G. Kang, and Y. Ni, "Electrically Conductive Fibre Composites Prepared from Polypyrrole-Engineered Pulp Fibres," *The Canadian Journal of Chemical Engineering,* vol. 83, pp. 896-903, 2005.

[20] C. D. Rouse, "Antenna Development for MIMO and UHF RFID Sytems," Ph.D., Electrical and Computer Engineering, University of New Brunswick, Fredericton, New Brunswick, 2014.

[21] L. J. van der Pauw, "A method of measuring specific resistivity and Hall effect of discs of arbitrary shape," *Philips Res. Rep.,* vol. 13, pp. 1-9, 1958.

[22] M. D. Pozar, *Microwave Engineering*, 3rd ed. Hoboken, NJ: John Wiley & Sons, Inc., 2005.

[23] I. U. and A. Inan, *Engineering Electromagnetics*. Menlo Park, California: Addison Wesley Longman Inc., 1999.

[24] C. Balanis, *Antenna Theory: Analysis and Design*. Hoboken, NJ: John Wiley & Sons Inc., 2005.

[25] M. Hotta, M. Hayashi, M. T. Lanagan, D. K. Agrawal, and K. Nagata, "Complex Permittivity of Graphite, Carbon Black and Coal Powders in the Ranges of X-band Frequencies (8.2 to 12.4 GHz) and between 1 and 10 GHz," *The Iron and Steel Institute of Japan,* vol. 51, pp. 1766-1772, 2011.

[26] M. Bolic, D. Simplot-Ryl, and I. Stojmenovic, *RFID Systems: Research Trends and Challenges*. Chicester, West Sussex, UK: John Wiley & Sons Ltd., 2010.

[27] P. Penfield, "Noise in Negative-Resistance Amplifiers," *Circuit Theory, IRE Transactions on,* vol. 7, pp. 166-170, 1960.

[28] K. Kurokawa, "Power Waves and the Scattering Matrix," *Microwave Theory and Techniques, IEEE Transactions on,* vol. 13, pp. 194-202, 1965.

[29] E. C. Jordan and K. G. Balmain, *Electromagnetic waves and radiating systems* vol. 4: Prentice-Hall Englewood Cliffs, NJ, 1968.

[30] M. Martinez-Moreno, C. A. Sanchez-Diaz, J. E. Gonzalez-Villarruel, G. Perez-Lopez, and B. Tovar-Corona, "Dipole Antenna Design for UHF RFID Tags," in *Electrical, Communications, and Computers, 2009. CONIELECOMP 2009. International Conference on*, Cholula, Puebla, 2009, pp. 220-224.

[31] K. D. Palmer and M. W. van Rooyen, "Simple broadband measurements of balanced loads using a network analyzer," *Instrumentation and Measurement, IEEE Transactions on*, vol. 55, pp. 266-272, 2006.

[32] I. Canada, "RSS-247 - Digital Transmission Systems (DTSs), Frequency Hopping Systems (FHSs) and Licence-Exempt Local Area Network (LE-LAN) Devices," ed, 2015.

[33] S. Uda and Y. Mushiake, *Yagi-Uda Antenna*. Tokyo, Japan: Sasaki Printing and Publishing Co., 1954.

[34] M. T. Reich and C. Bauer-Reich, "UHF RFID impedance matching: When is a T-match not a T-match?," in *RFID (IEEE RFID), 2014 IEEE International Conference on*, Orlando, FL, 2014, pp. 23-30.

[35] G. Marrocco, A. Fonte, and F. Bardati, "Evolutionary design of miniaturized meander-line antennas for RFID applications," in *Antennas and Propagation Society International Symposium, 2002. IEEE*, San Antonio, TX, 2002, pp. 362-365 vol.2.

[36] P. V. Nikitin and K. V. S. Rao, "Effect of Gen2 protocol parameters on RFID tag performance," in *RFID, 2009 IEEE International Conference on*, Orlando, FL, 2009, pp. 117-122.

Appendix A Ancillary Tables and Graphs

Table A.1: Impedances and sensitivties of various commercial EPC Class 1 Gen 2 passive UHF RFID ICs.

Manufacturer	IC Model	Parallel Equivalent Input Resistance (Ω)	Parallel Equivalent Input Capacitance * (pF)	Parallel Equivalent Input Impedance at 915 MHz (Ω)	Series Equivalent Input Impedance at 915 MHz (Ω)	Read Sensitivity (dBm)
Impinj	Monza 4	1650	1.21	1650-j143.8	12.4-j142.7	-17.4
Impinj	Monza 5	1800	1.07	1800-j162.6	14.6-j161.3	-17.8
Impinj	Monza R6	1200	1.44	1200-j120.8	12.0-j119.6	-20.0
Alien Technology	Higgs 3	1500	0.85**	1500-j204.6	27.4-j200.9	-18.0
Alien Technology	Higgs 4	1800	0.95	1800-j183.1	18.4-j181.2	-18.5
NXP Semiconductors	UCODE G2iL	-	0.77**	-	23-j224	-18.0
NXP Semiconductors	UCODE G2iM	-	0.77**	-	24-j222	-17.5
NXP Semiconductors	UCODE 7	-	0.63**	-	12.5-j277	-20.0

** Additional parasitic capacitances from antenna mounting and chip packages are included in this value.*
*** Value is reported for bare IC die alone.*

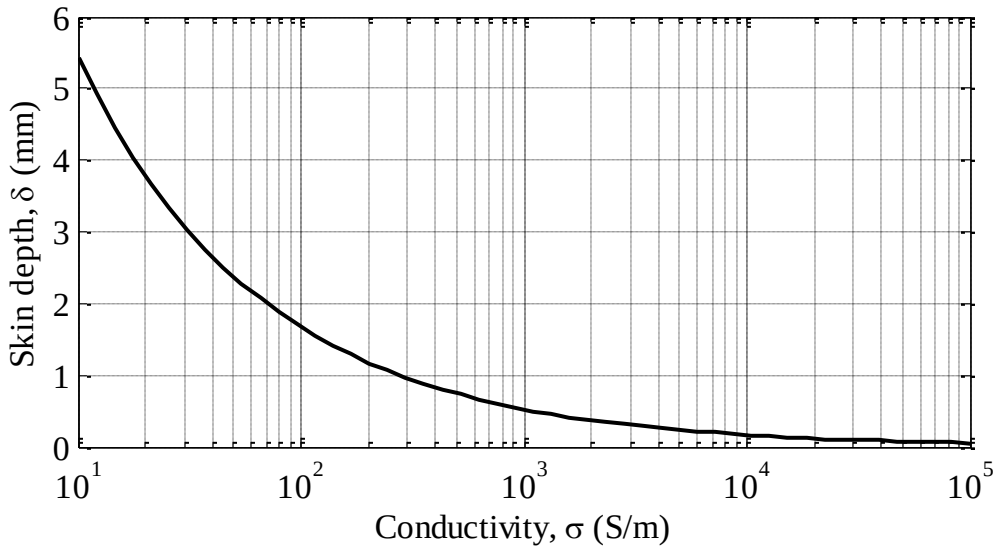

Figure A.1: Skin/Penetration depth in a conductor as a function of conductivity.

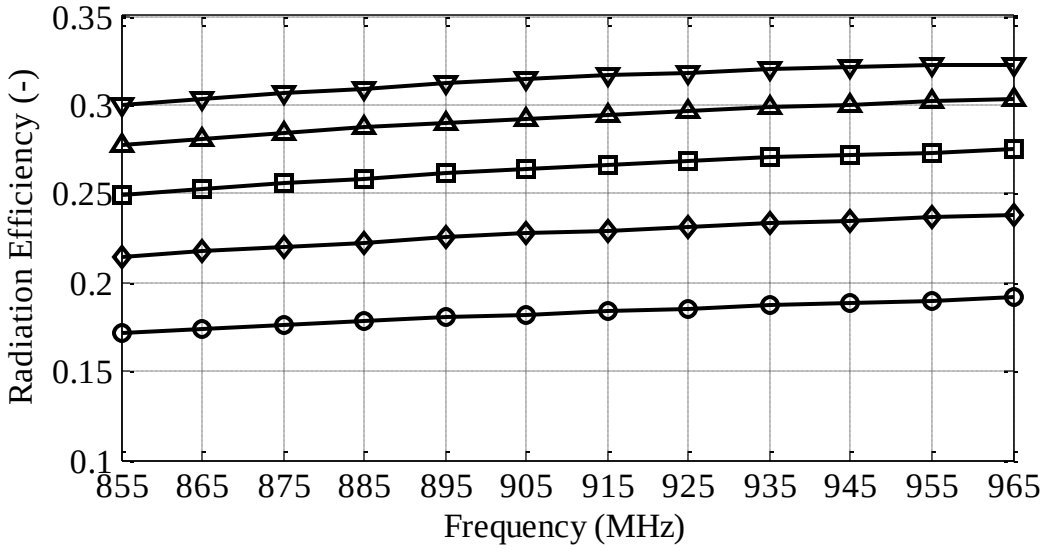

Figure A.2: Simulated radiation efficiencies for 164 mm long graphite-ink dipoles of various widths. ○: w = 6 mm, ◇: w = 8 mm, □: w = 10 mm, △: w = 12 mm, ▽: w = 14 mm.

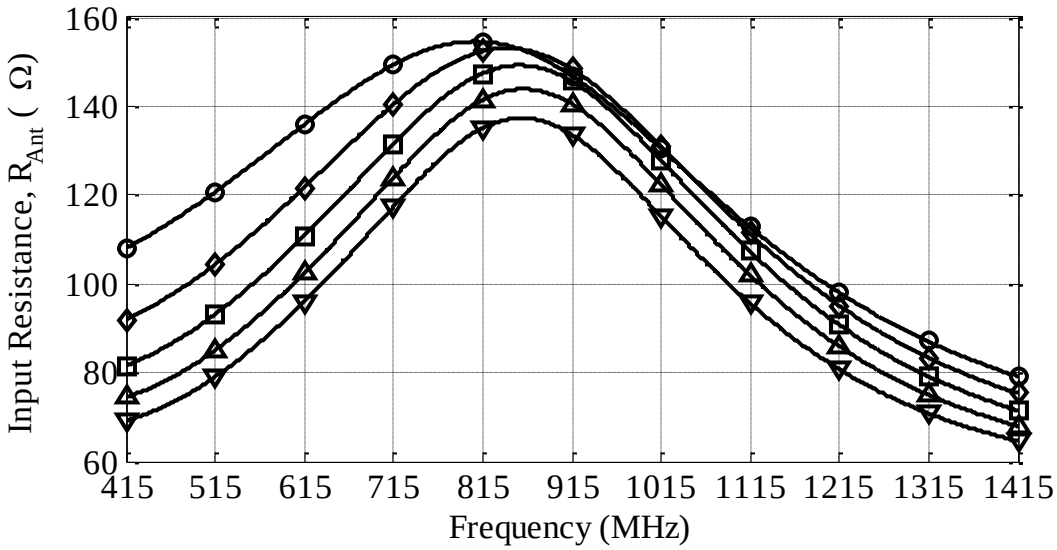

Figure A.3: Simulated input resistances for 164 mm long graphite-ink dipoles of various widths. ○: w = 6 mm, ◇: w = 8 mm, □: w = 10 mm, △: w = 12 mm, ▽: w = 14 mm.

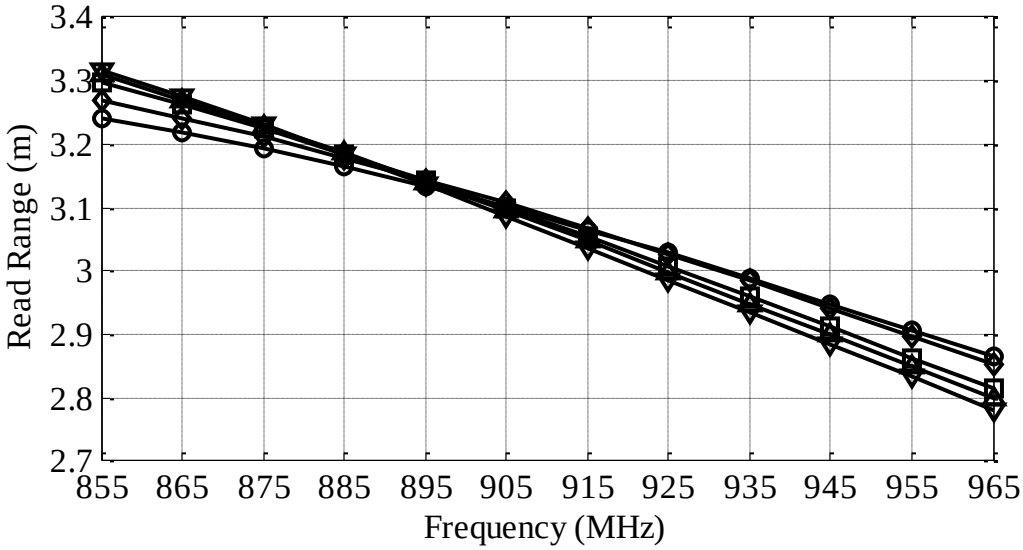

Figure A.4: Full frequency span simulated read ranges for 10 mm wide graphite-ink dipoles of various lengths. ○: l = 149 mm, ◇: l = 152 mm, □: l = 155 mm, △: l = 158 mm, ▽: l = 161 mm.

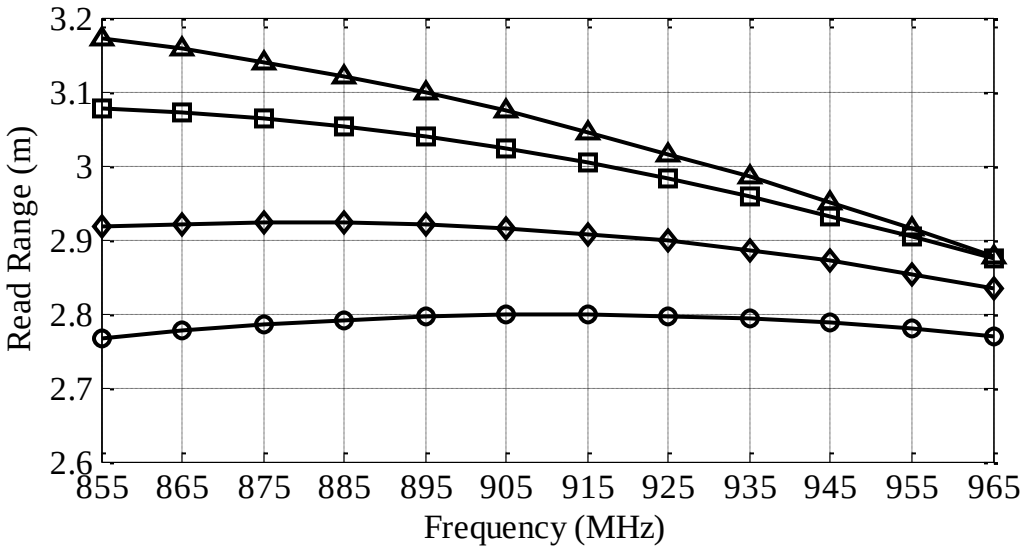

Figure A.5: Simulated read ranges for 10 mm wide graphite-ink dipoles of various lengths. ○: l = 125 mm, ◇: l = 131 mm, □: l = 137 mm, △: l = 143 mm.

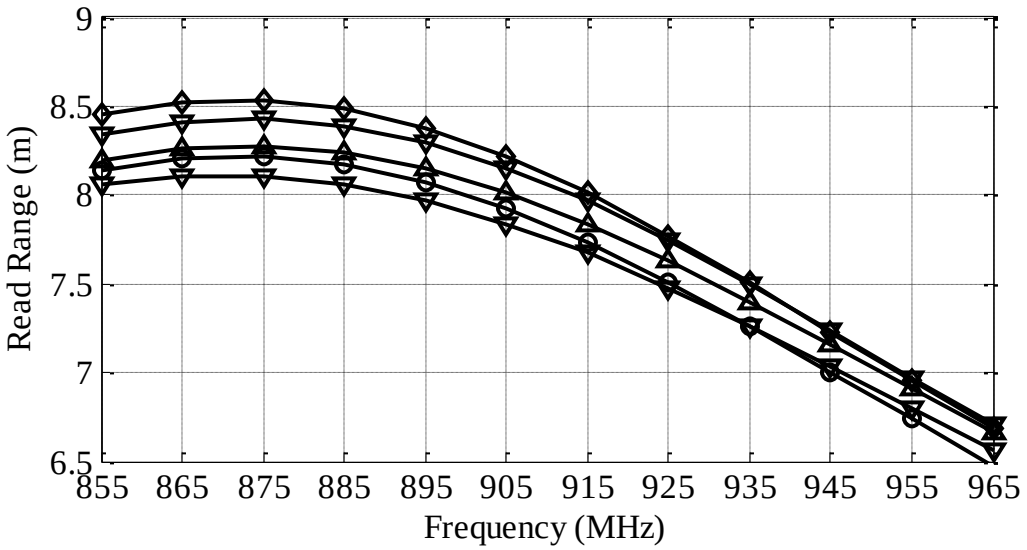

Figure A.6: Full frequency span simulated read ranges for 164 mm long exfoliated-graphite dipoles of various widths. ○: w = 1 mm, ◇: w = 3 mm, □: w = 5 mm, △: w = 7 mm, ▽: w = 9 mm.

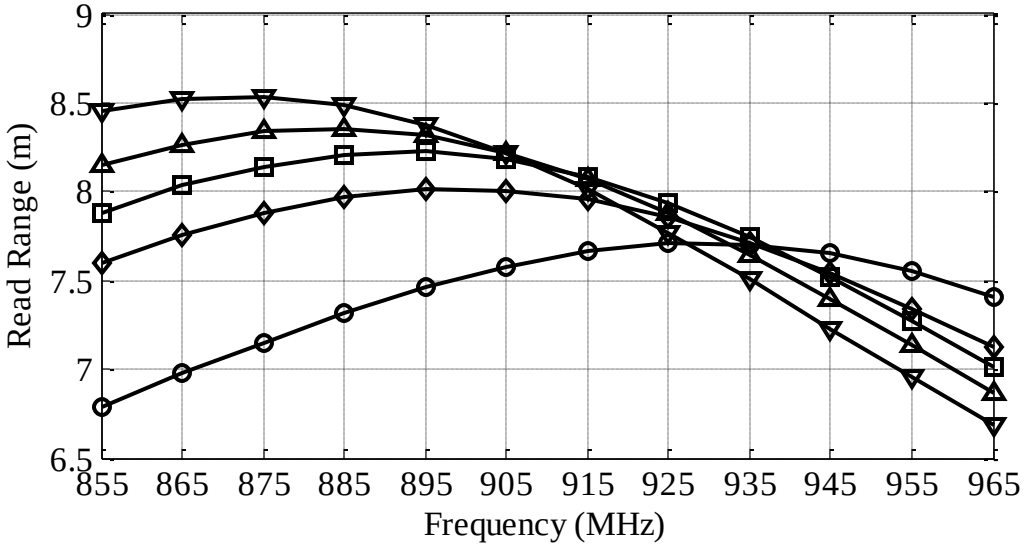

Figure A.7: Full frequency span simulated read ranges for 3 mm wide exfoliated-graphite dipoles of various lengths. ○: l = 152 mm, ◇: l = 155 mm, □: l = 158 mm, △: l = 161 mm, ▽: l = 164 mm.

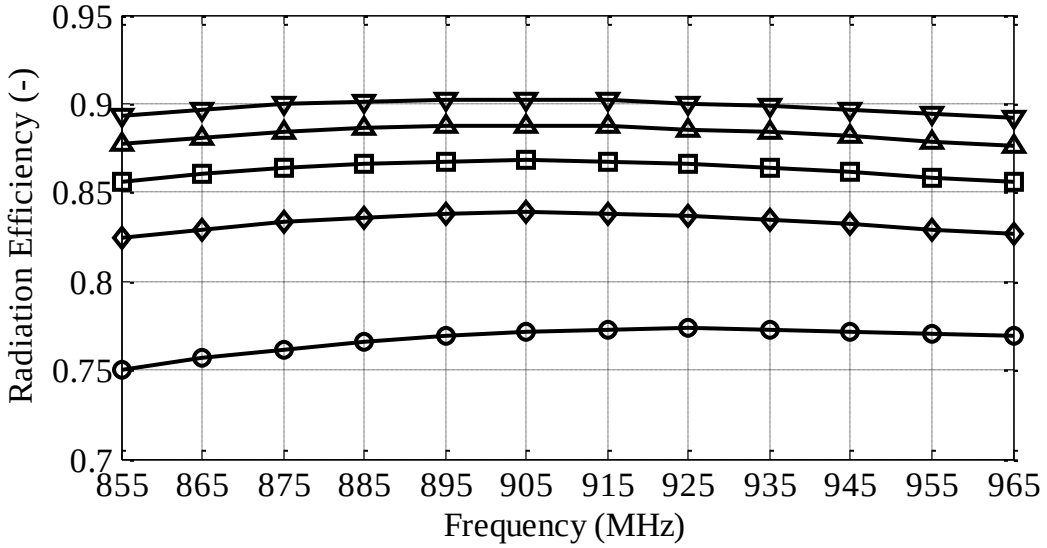

Figure A.8: Simulated radiation efficiencies for 164 mm long exfoliated-graphite dipoles of various widths. ○: w = 1 mm, ◇: w = 3 mm, □: w = 5 mm, △: w = 7 mm, ▽: w = 9 mm.

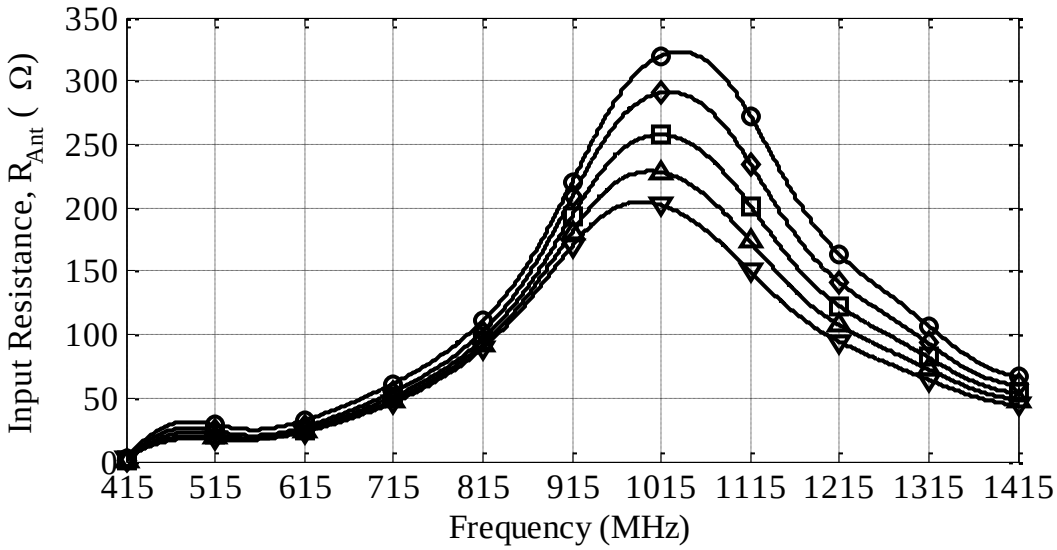

Figure A.9: Simulated input resistances for 164 mm long exfoliated-graphite dipoles of various widths. ○: w = 1 mm, ◇: w = 3 mm, □: w = 5 mm, △: w = 7 mm, ▽: w = 9 mm.

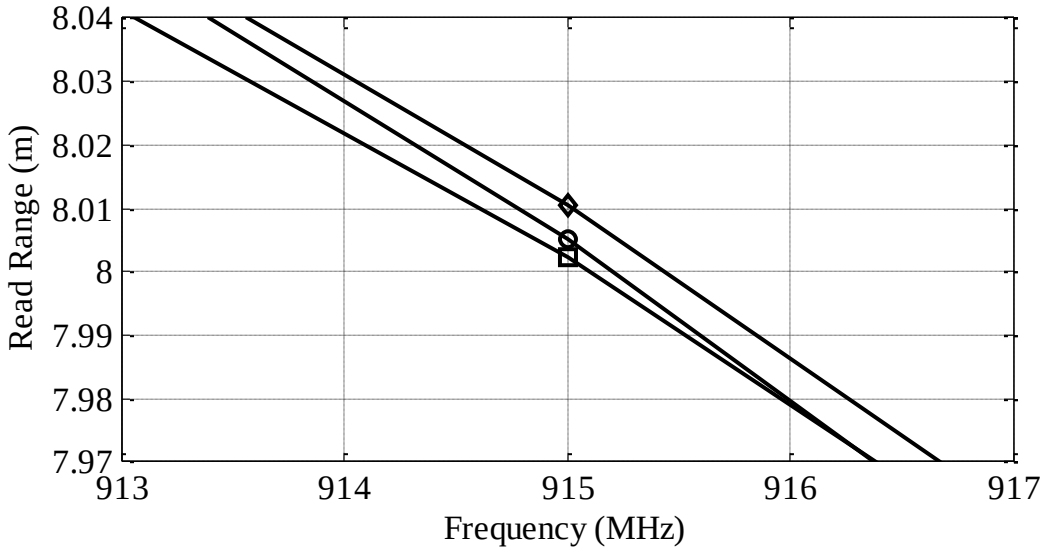

Figure A.10: Simulated read ranges for 164 mm long exfoliated-graphite dipoles of various widths. ○: w = 2 mm, ◇: w = 3 mm, □: w = 4 mm.

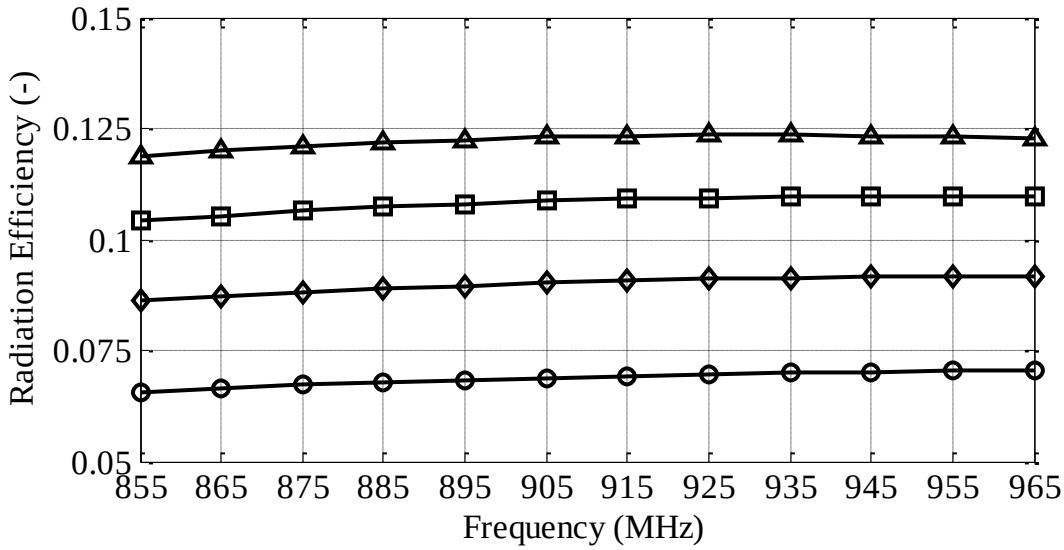

Figure A.11: Simulated radiation efficiencies for graphite-ink T-match dipoles for various lengths of l_2 with s_e = 11. ○: l_2 = 30 mm, ◇: l_2 = 40 mm, □: l_2 = 50 mm, △: l_2 = 60 mm.

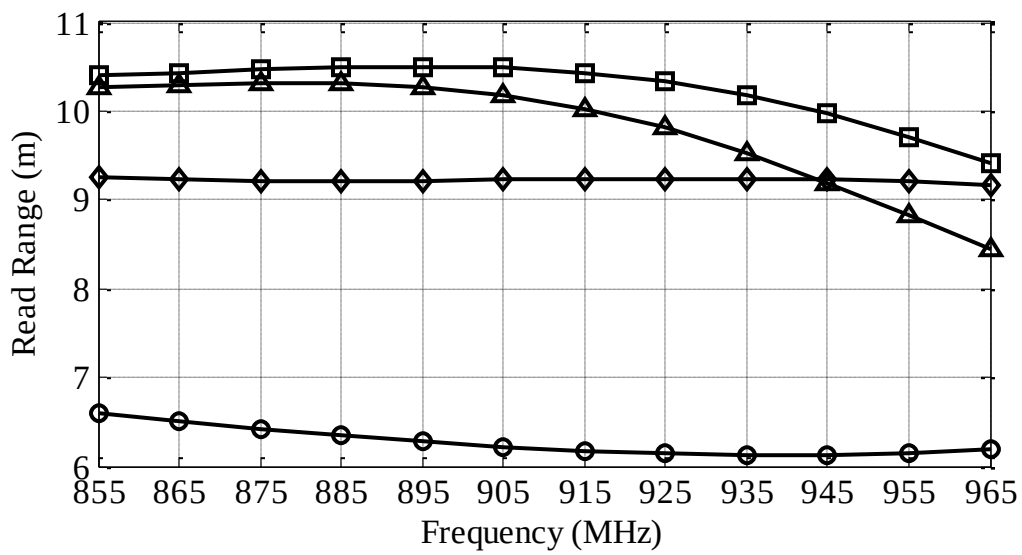

Figure A.12: Simulated read ranges for exfoliated-graphite T-match dipoles for various lengths of l_2 with s_e = 5. ○: l_2 = 30 mm, ◇: l_2 = 40 mm, □: l_2 = 50 mm, △: l_2 = 60 mm.

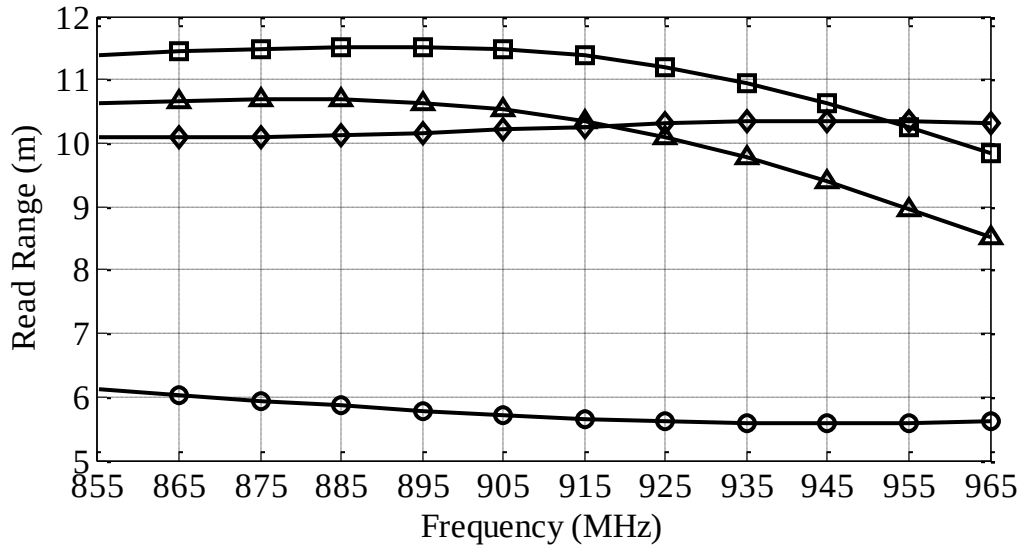

Figure A.13: Simulated read ranges for graphite-ink T-match dipoles for various lengths of l_2 with s_e = 7. ○: l_2 = 20 mm, ◇: l_2 = 30 mm, □: l_2 = 40 mm, △: l_2 = 50 mm.

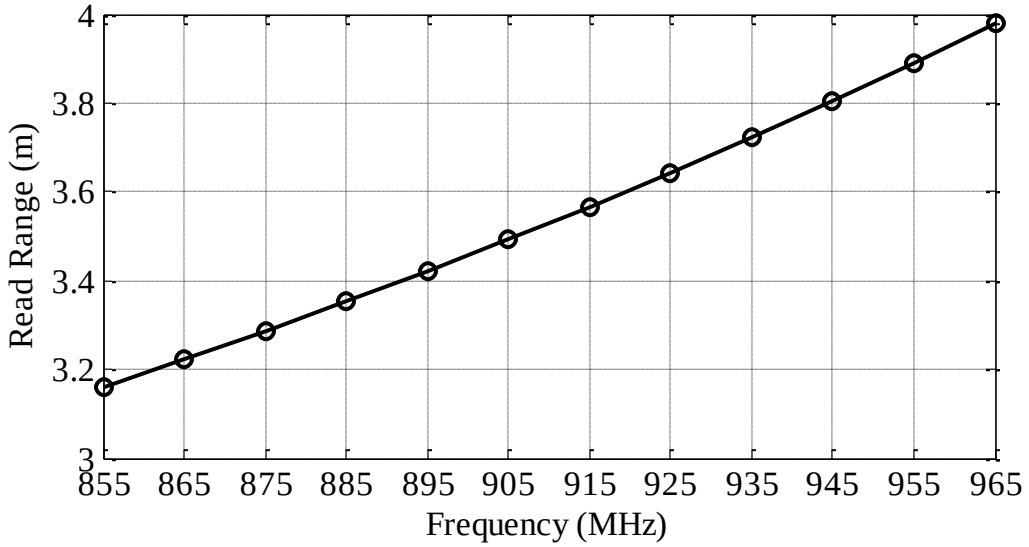

Figure A.14: Simulated read ranges for exfoliated-graphite MLA with N=5 meanders.

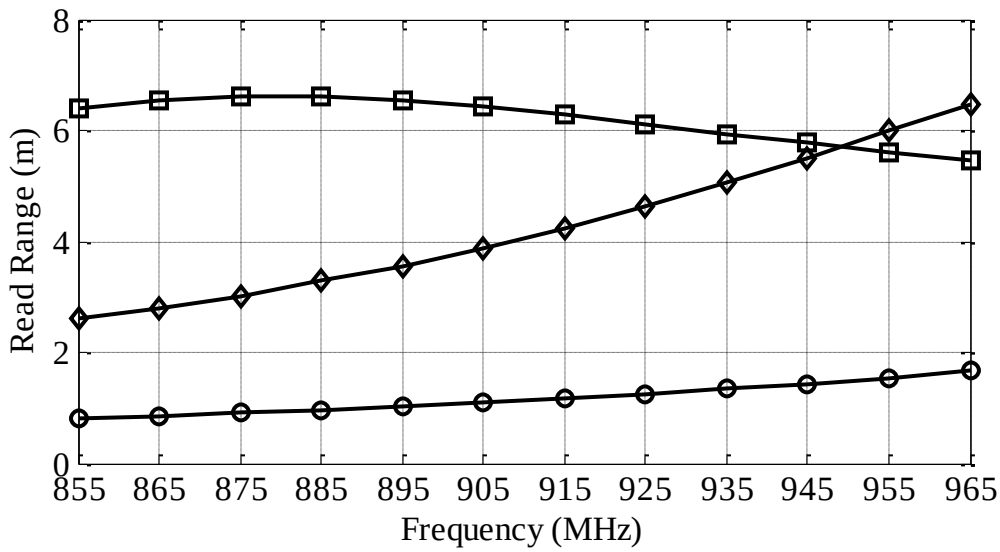

Figure A.15: Simulated read ranges for exfoliated-graphite MLA with a T-match for various lengths of l_2 with s_e = 7 and N = 6. ○: l_2 = 10 mm, ◇: l_2 = 20 mm, □: l_2 = 30 mm.

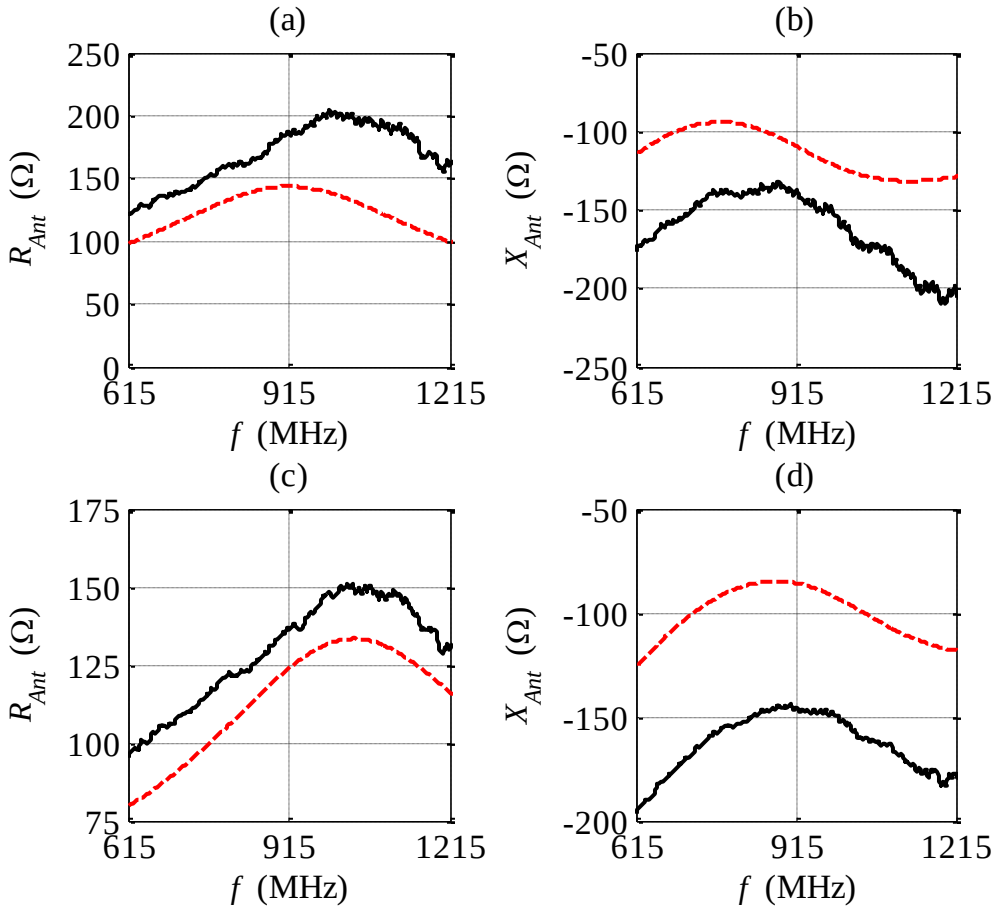

Figure A.16: Measured and simulated input impedances for optimized 152 mm (a-b) and 131 mm long (c-d) graphite-ink dipoles. Solid: measurement, dashed: simulation.

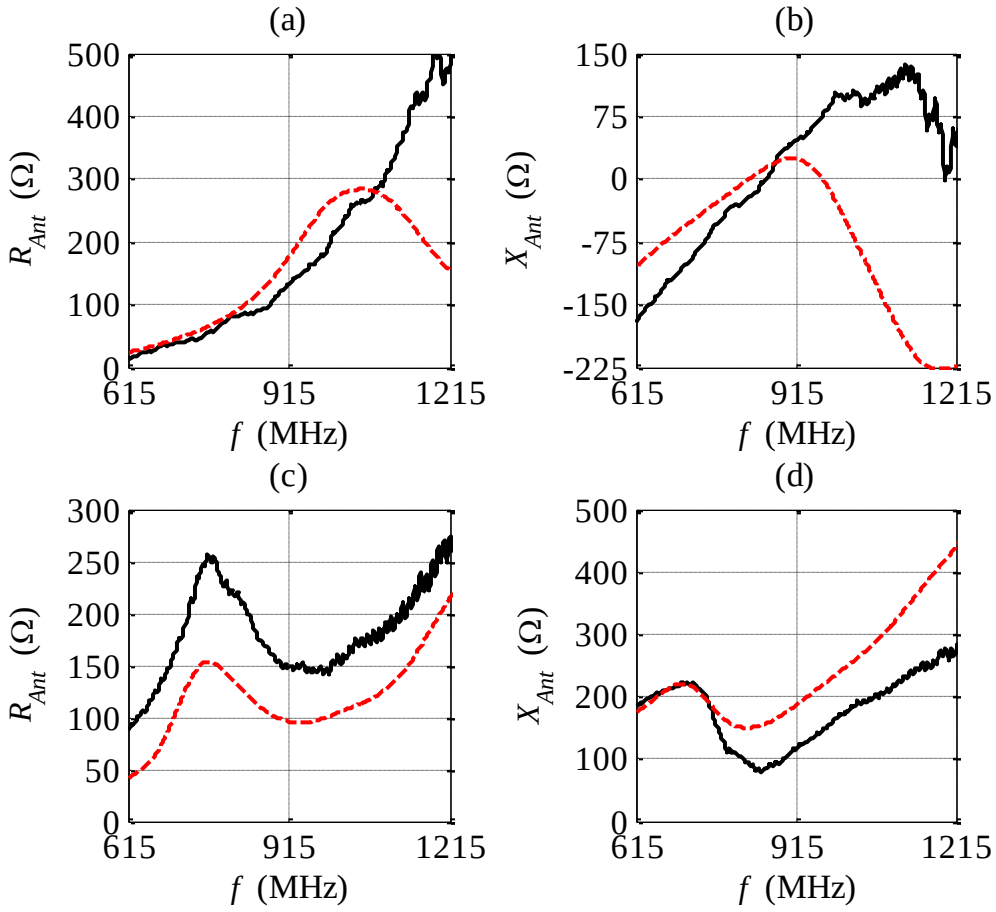

Figure A.17: Measured and simulated input impedances for optimized 158 mm long exfolaited-graphite dipole (a-b) and T-match antennas (c-d). Solid: measurement, dashed: simulation.

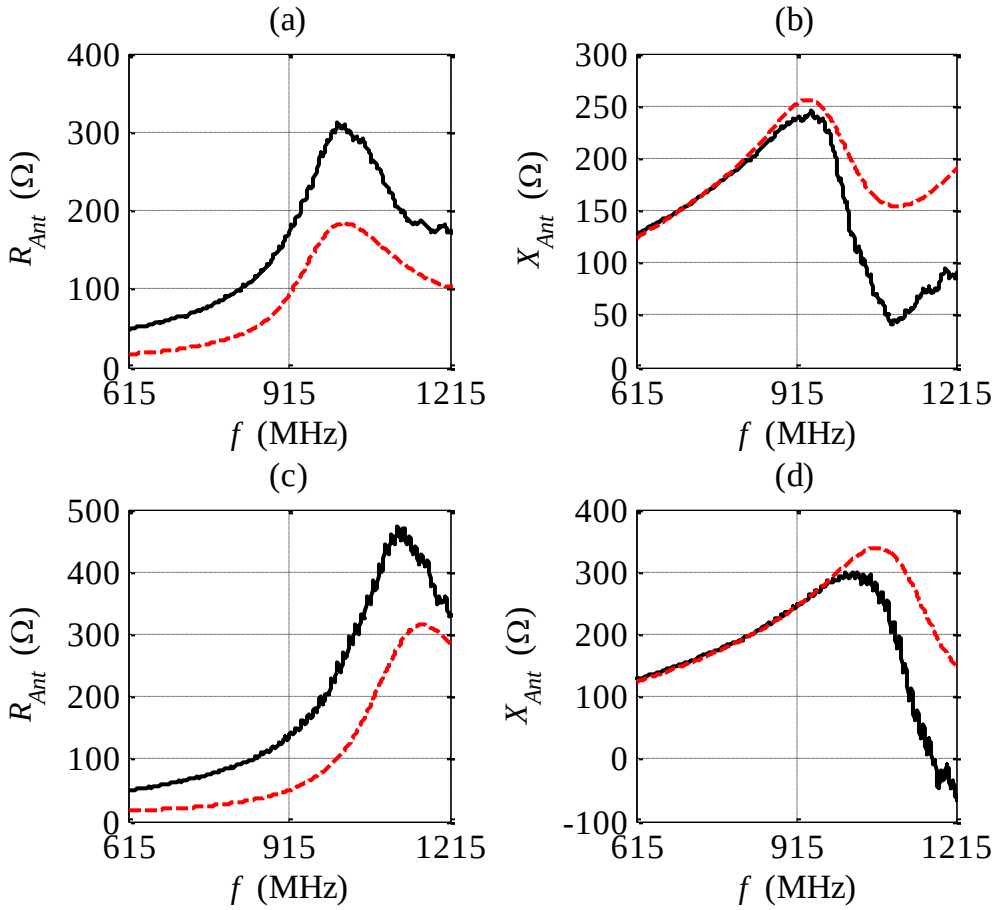

Figure A.18: Measured and simulated input impedances for optimized N = 5 (a-b) and N = 6 (c-d) graphite-ink MLAs. Solid: measurement, dashed: simulation.

Appendix B Antenna Stencils

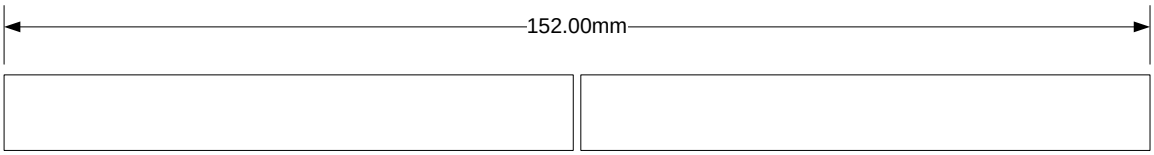
152.00mm

A

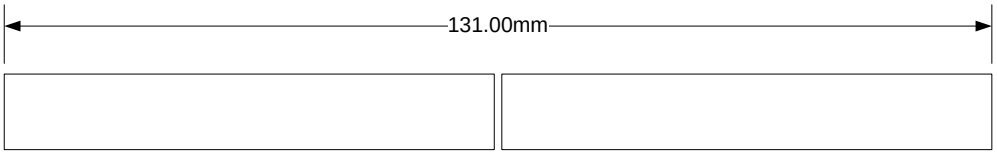
131.00mm

B

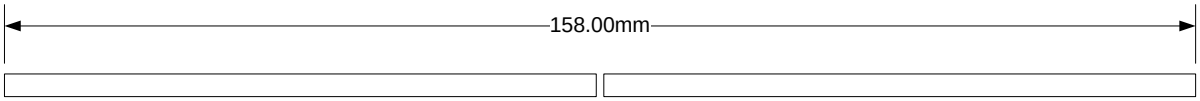
158.00mm

C

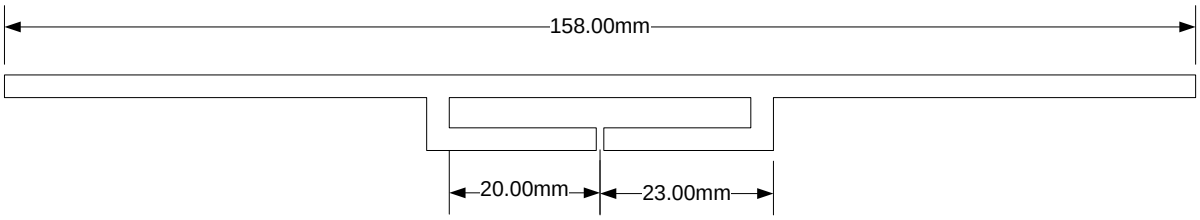
158.00mm
20.00mm
23.00mm

D

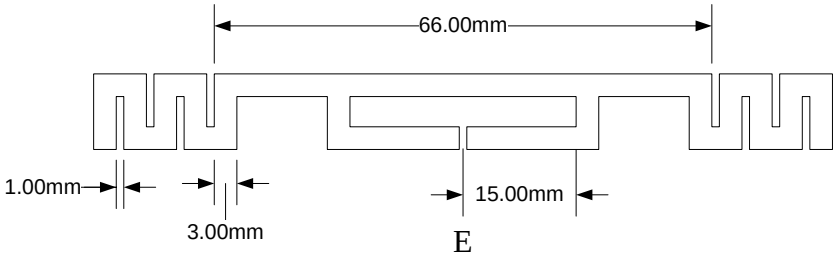
66.00mm
1.00mm
3.00mm
15.00mm

E

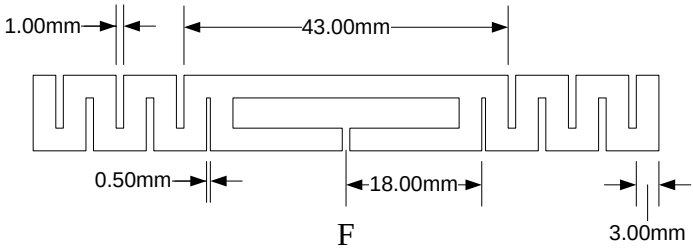
1.00mm
43.00mm
0.50mm
18.00mm
3.00mm

F

Curriculum Vitae

Candidate's full name: Michael Robert Kurz

Universities attended: University of New Brunswick, B.Sc.E., 2012

Publications:

Chris D. Rouse, Michael R. Kurz, Brent R. Petersen, and Bruce G. Colpitts, "Performance analysis of conductive paper antennas," *IEEE Transactions on Antennas and Propagation*, vol. 61, no. 3, pp. 1427-1430, March 2013.